*SACLANT UNDERSEA
RESEARCH CENTRE
REPORT*

ON THE APPLICABILITY OF SATELLITE - BORNE **SAR** IMAGERY TO COASTAL OCEANOGRAPHY

H. H. Essen

February 1996

NORTH ATLANTIC TREATY ORGANIZATION

SACLANTCEN SR-247

On the applicability of satellite-borne SAR imagery to coastal oceanography

H.-H. Essen

The content of this document pertains to work performed under Project 23 of the SACLANTCEN Programme of Work. The document has been approved for release by The Director, SACLANTCEN.

Director

intentionally blank page

SACLANTCEN SR-247

On the applicability of satellite-borne SAR imagery to coastal oceanography

H.-H. Essen

Executive Summary: In recent years the rapid assessment of unknown areas has become one of the main research tasks at SACLANTCEN. It is apparent that satellite remote sensing is an appropriate tool for this purpose. For rapid environmental assessment, increasing attention has been paid to relating satellite surface measurements to the subsurface structure of the oceans in close assosiaton with environmental and acoustic research at the Centre. The application of satellite remote sensing to coastal waters requires sensors of high resolution. From space, ocean colour and sea-surface temperature may be measured with a resolution of about 1 km.

The first European Space Agency (ESA) remote sensing satellite (ERS-1), launched in July 1991, carries among other instruments a synthetic aperture radar (SAR). This C-band SAR takes high-resolution (about 30 m) images of 100 × 100 km areas. Unlike sensors operating in the visible or infrared band, the microwave SAR is not affected by cloud cover. It is an active instrument which does not require day light. The radar wavelength used (5.7 cm) penetrates only by a fraction of the wavelength into seawater, which means that subsurface features can only be sensed indirectly *via* their expression in sea-surface roughness, which causes the radar backscatter. Nevertheless, SAR images reveal remarkable capabilities of imaging mesoscale oceanic features.

This report investigates SAR images of ERS-1, which have been acquired in support of SACLANTCEN's oceanographic work. Emphasis is on mesoscale processes and the extent to which quantitative information can be obtained from SAR images. By making use of empirical relationships between wind speed and the radar cross section, wind speed has been calculated from SAR images and compared with *in situ* data. The capability of imaging thermal fronts has been investigated by applying theories of boundary-layer stability and SAR imagery to satellite-measured sea-surface temperatures. The possibility of determining changes in surface current from SAR images is emphasized.

Although the feasibility of extracting quantitative information from SAR images is demonstated in this report, limitations arise from the unsufficient knowledge of oceanographic parameters needed and the impossibility of separating different physical processes affecting SAR imagery. However, with supplementary information from other satellite sensors and/or *in situ* measurements, SAR images contribute to an impoved understanding of mesocale processes in the ocean.

intentionally blank page

SACLANTCEN SR-247

On the applicability of satellite-borne SAR imagery to coastal oceanography

H.-H. Essen

Abstract: Synthetic aperture radar (SAR) images have been acquired from the first European Space Agency (ESA) remote sensing satellite ERS-1. The mesoscale feature images are from Norwegian coastal waters and the Mediterranean (Elba and Sicily areas). Theories are tested for their ability to explain the observed variability of the radar-cross section. By means of empirical models, developed for the ERS-1 scatterometer, wind speeds are extracted from the SAR images and compared with measured data. Theories of SAR imaging and boundary-layer stability are applied to investigating the imaging of thermal fronts. The possibility of determining surface-current variability from SAR images is emphasized. The theoretical approach is based on the modulation of small-scale scattering waves by underlying currents.

Keywords: C-band SAR – coastal oceanography – ERS-1 – surface current surface wind – thermal fronts

Contents

1

Introduction

The first European Space Agency (ESA) remote sensing satellite (ERS-1), launched in July 1991, carries among other instruments a synthetic aperture radar (SAR). This C-band SAR takes high-resolution (about 30 m) 100×100 km images of the sea-surface. The SAR uses satellite motion to form a long synthetic antenna from a smaller real one. The Doppler shift of the scattered signal is used to obtain azimuth resolution. It is assumed that the targets are stationary and that the Doppler shift is due entirely to the radar motion. Short pulses are transmitted in order to obtain approximately the same resolution in range as in azimuth.

Unlike sensors operating in the visible or infrared bands, the microwave SAR is not affected by cloud cover. It is an active instrument which does not require day light. SARs are operated from aircrafts and satellites at angles of incidence, where the backscattering strength, i.e. the radar cross section, depends primarily on the small-scale roughness of the sea surface. Short surface waves are generated by the wind field and may be affected by surface slicks and underlying oceanic processes. Many SAR images clearly show ocean swell, and great effort has been expended on determining the two-dimensional wave-height spectrum. The main problem in this context is that the motion of the sea surface distorts the SAR imaging process.

The L-band SAR of Seasat (in operation for 100 days in 1978) demonstrated remarkable capabilities for imaging mesoscale sea-surface features. The subsequent lack of space-borne SAR data limited the development of SAR application to oceanography until the launch of ERS-1 [1]. The paper cited discusses some examples of SAR images taken from ERS-1 showing mesoscale oceanic variability. The presence of an eddy is indicated by dark spiral lines, which are interpreted as organic material aligned in the orbital motion of the eddy. An AVHRR image of sea-surface temperature and a sequence of three SAR images from Norwegian coastal waters reveal remarkable relationships. The SAR image expressions are interpreted as wave-current interactions along the current (thermal) front.

Meteorological and oceanographic processes as observed in SAR images of ERS-1 have been summarized by [2] and are presented in Table 1 in conjunction with the ranges of wind speed at which these processes become visible. The lower wind-speed limit for imagery with the C-band SAR of ERS-1 is about 3 ms^{-1}.

feature	wind speed (ms^{-1})	
	minimum	maximum
atmospheric waves	3	15
rain cells	3	14
wind vector	3	21
wind waves, swell	7	18
eddies, current fronts	3	12
oil spills	3	10
natural films	3	8

Table 1 *Wind speed dependence of atmospheric and oceanic feature visibility in SAR images, from: Johannessen et al. [2].*

This report investigates SAR images of ERS-1, which have been acquired in support of SACLANTCEN's oceanographic work. Emphasis is placed on mesoscale processes and the extent to which quantitative information can be obtained from SAR images. The radar wavelengths used penetrate only by a fraction of the wavelength into seawater, which means that subsurface features can only be sensed indirectly *via* the modulation of the short surface waves. Theories explaining the features visible in SAR images are based on the following physical processes: horizontal variability of surface winds, instability of the atmospheric boundary layer, i.e. of the air-sea temperature difference (not mentioned in Table 1), surface current variability, and modulation of short waves by the presence of slicks.

In order to validate theoretical approaches, SAR images were selected for which ground truth data are available. The imaging of swell and the influence of surface slicks are not investigated. It is assumed that the distortion of SAR imagery due to the motion of the surface (velocity bunching) can be disregarded. Wind speeds are extracted from SAR images by means of empirical models, developed for the C-band scatterometer of ERS-1, and compared with *in situ* data. The reproduction of thermal fronts in SAR images is investigated by comparison with satellite images (AVHRR) of sea-surface temperature. For quantitative results, theories of boundary-layer stability and SAR imaging are applied. Underlying surface currents modulate the small-scale scattering waves and in turn the radar-cross section. For the C-band, this mechanism underestimates the radar-cross section variability. More realistic values are found when taking into account the influence of intermediate surface waves, which are longer than the scattering waves but shorter than the SAR resolution.

The feasibility of extracting quantitative information from SAR images only is limited by the lack of sufficiently accurate parameters, required by theory, as for example the intermediate wave spectrum. A complicating factor is that observed features may be a result of more than one process, e.g. if a thermal front coincides with a current front.

2

SAR imagery of the sea surface

A short review is given of the physical processes affecting SAR imagery of the sea surface. SAR normally operates at incidence angles between 20° and 60°. Bragg scattering is generally accepted to be the dominant imaging mechanism in this range, and scattering coefficients can be derived by means of first-order perturbation theory. For smaller incidence angles, specular reflection from sloping surface elements has to be taken into account and for larger incidence angles, shadowing effects become important.

It is assumed that the satellite propagates in y-direction and the radar beam is transmitted parallel to the x-axis, i.e. to the right of the satellite track (Fig. 1).
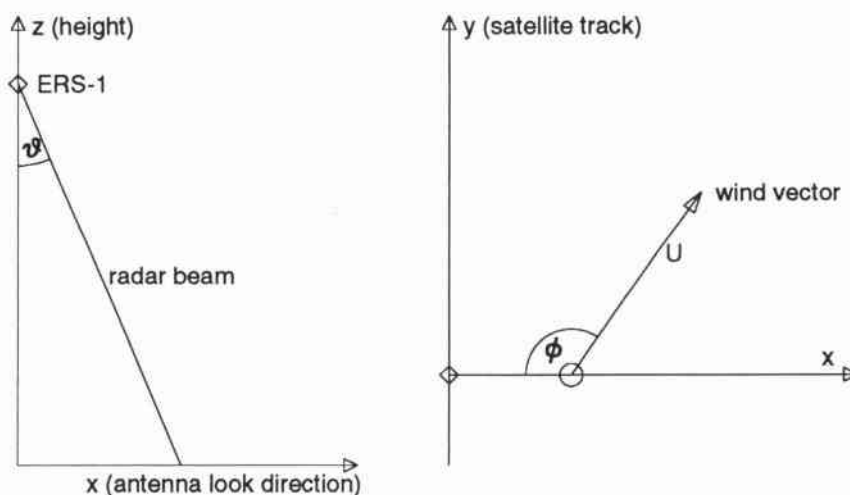
Figure 1: *Geometry of the space-borne SAR. The left panel shows the vertical plane through the radar beam, and the right panel the sea surface. The x-axis is parallel to the antenna look direction. The wind direction is clockwise and zero when the wind blows towards the radar. The instantaneously observed area is indicated by a circle.*

Then, the Bragg condition reads,

$$\mathbf{k}_b = \pm 2\mathbf{k}_r \quad with, \quad \mathbf{k}_r = \frac{2\pi\nu}{c}[1,0]\sin\vartheta, \tag{1}$$

where $\mathbf{k}_r$ is the horizontal radar wavevector, ν is the radar frequency, c the velocity

of light, and ϑ the incidence angle of the radar beam. $\mathbf{k}_b$ is the two-dimensional vector of surface waves responsible for backscattering. Thus, backscattering is due to surface waves with wavelengths $\lambda_b = c/(2\nu \sin \vartheta)$, propagating parallel or antiparallel to the horizontal projection of the radar beam. For the SAR of ERS-1, operating at $\nu = 5.3$ GHz with incidence angles ϑ between 20° and 26°, the range of scattering surface wavelengths extends from 8.2 cm to 6.5 cm, respectively.

Short surface waves in the range mentioned fulfill the dispersion relation,

$$\omega^2 = gk + \frac{\kappa k^3}{\rho}, \tag{2}$$

where ω is the circular frequency and k the modulus of the two-dimensional wave vector, $g = 9.8$ ms^{-2} is the gravity acceleration, $\kappa = 0.072$ kgs^{-2} the surface tension and $\rho = 1000$ kgm^{-3} the density of water. For the wavelengths under consideration the influence of gravity dominates but surface tension can not be disregarded. At the wavelength of $\lambda = 2\pi/k = 7.5$ cm, the wave period is $T = 2\pi/\omega = 0.21$ s, the phase velocity $v_p = \omega/k = 0.35$ ms^{-1}, and the group velocity $v_g = d\omega/dk = 0.19$ ms^{-1}, i.e. somewhat higher than half of the phase velocity, as it would be in the case of pure gravity waves.

The Bragg scattering theory determines the dependence of the normalized radar cross section σ_o on the two-dimensional wave height spectrum $F(\mathbf{k})$ of the frozen sea surface, which contains the contributions of both components $+2\mathbf{k}_r$ and $-2\mathbf{k}_r$ in Eq. (1),

$$\sigma_o = T(\vartheta)F(\mathbf{k}_b). \tag{3}$$

In addition, the coefficient T depends on the complex dielectric constant of the water illuminated and on the polarisation of the transmitted and received signals, which are both vertical for the SAR of ERS-1. In this case, one obtains [3],

$$T(\vartheta) = 4\pi \left(\frac{2\pi\nu \cos \vartheta}{c}\right)^4 \left|\frac{(1 - \epsilon)[\epsilon(1 + \sin^2 \vartheta) - \sin^2 \vartheta]}{(\epsilon \cos \vartheta + \sqrt{\epsilon - \sin^2 \vartheta})^2}\right|^2. \tag{4}$$

The dielectric constant ϵ varies with the radar frequency and depends on the salinity and temperature of the water. Some values at 5.3 GHz, as extracted from the curves of Ulbay et al. [4] are presented in Table 2.

temperature	pure water	sea water
0°C	68 - 36i	60 - 42i
20°C	75 - 21i	68 - 32i

Table 2 *Complex dielectric constants at 5.3 GHz of pure water and sea water for two temperatures, from: Ulbay et al. [4].*

Because of the difficulties in obtaining measurements, little is known of the two-dimensional wave-height spectrum at short wavelengths. The equilibrium frequency-

spectrum of Phillips [5] is independent of wind speed. Assuming a $\cos^2$-distribution of directions around the mean wind and transforming to the wave-vector space, the contributions in Eq. (3) from waves moving parallel and antiparallel to the x-axis become,

$$F(\mathbf{k}_b) = 0.008k^{-4}\cos^2\phi, \tag{5}$$

where ϕ is the mean wind direction as defined in Fig. 1, i.e. referring to the radar beam. The amplitude in Eq. (5) is only an approximate value, as it has been deduced from measurements at longer wavelengths than considered here. Figure 2 displays radar cross sections as obtained by Eqs. (3)-(5). It has been assumed that the wind is blowing towards the radar, i.e. $\phi = 0$. The curves computed with the dielectric constants of Table 2 are virtually identical. This means that variations of the dielectric constant may be disregarded with respect to backscatter from the sea surface. The dashed line refers to an infinite conductivity, which yields considerably higher radar cross sections. Thus, the assumption of infinite conductivity, which is sometimes used to simplify Eq. (4), leads to false estimates of σ_o.
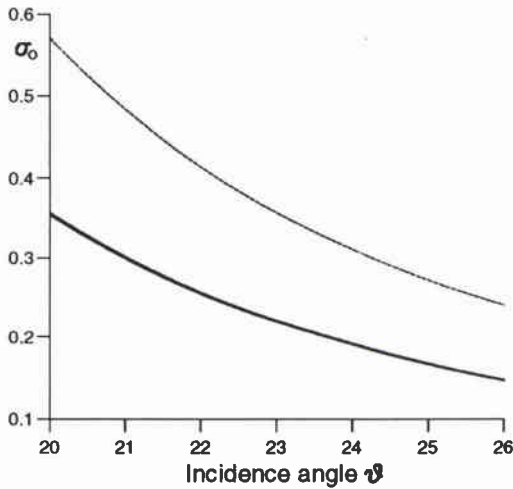
Figure 2: *Radar cross section σ_o as function of incident angle ϑ for the four dielectric constants of Table 1 (solid line) and infinite conductivity (dashed line), derived by means of Bragg theory, Eqs. (3)-(4), with Phillips spectrum, Eq. (5), and wind blowing towards the radar ($\phi = 0$).*

2.1 Surface winds

It is known that short surface waves respond quickly to local winds. In contrast to the equilibrium spectrum, Eq. (5), the real spectrum has to be considered as wind-dependent. Radar cross sections measured by scatterometers are used to determine near-surface winds. For this purpose, empirical formula have been developed, which

describe σ_o as a function of wind speed and direction at a certain reference height (usually 10 m) in a neutrally stratified atmospheric boundary layer. In addition to the radar frequency and polarisation, these formula contain dependencies on the vertical incidence angle (ϑ in Fig. 1) and wind direction relative to the radar beam (ϕ in Fig. 1).

On ERS-1, scatterometer and SAR operate at the same frequency. Thus, the so-called σ_o-models derived for the scatterometer are also applicable to the SAR. In principle, the SAR can be considered as a high-resolution scatterometer. Figure 3 displays the radar cross section for four different wind speeds as a function of the incidence angle ϑ (left panel) and wind direction ϕ relative to the radar (right panel). Two different σ_o-models have been used, that of IFREMER and CMOD4 of ESA (Annex A).
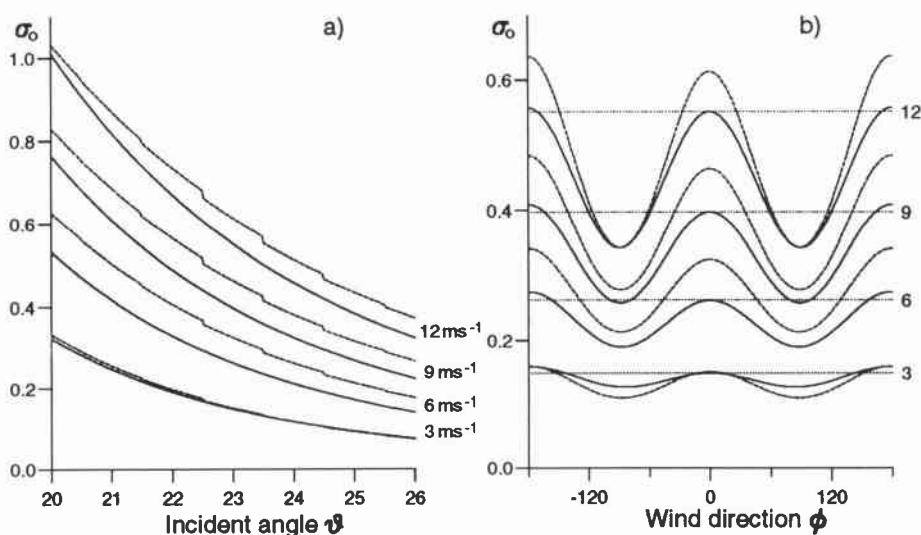
Figure 3: *Radar cross-section σ_o for different wind speeds, as given by the σ_o-models of IFREMER (full lines) and CMOD4 (dashed lines): a) dependence on incidence angle ϑ for wind blowing towards the radar ($\phi = 0$), b) dependence on wind direction ϕ relative to the radar at the incidence angle of $\vartheta = 23°$.*

For the dependence on incidence angle (left panel of Fig. 3), it has been assumed that the wind blows towards the radar ($\phi = 0$). Considerably higher σ_o-values are found for wind speeds exceeding some 5 ms^{-1} than predicted by the equilibrium spectrum, Eq. (5). In addition, the decrease of σ_o with incidence angle is stronger than theoretically expected. The dependence of σ_o on the wind direction (right panel of Fig. 3) refers to an incidence angle of $\vartheta = 23°$. The radar cross section is smaller for winds perpendicular to the radar beam, but does not vanish as predicted by Eqs. (4) and (5).

Figure 3 indicates that the two-dimensional waveheight spectrum is more complex than assumed in Eq. (5). Indeed, the σ_o-models may be used to estimate more realistic spectra. Obviously, the two σ_o-models show differences for both the dependence on wind speed and direction. For the purpose of determining wind speeds from σ_o this is of some importance. But the more serious problem is that in general, the wind direction is not known, which leads to a high uncertainty mainly for higher wind speeds. For low wind speeds, e.g. 3 ms^{-1}, the IFREMER model varies only slightly with wind direction.

2.2 Sea surface temperatures

Under certain conditions, SAR images are able to map spatial changes in sea-surface temperature (SST). Askari et al. [6] explain this effect by the assumption that σ_o is a function of the wind stress τ rather than the wind speed U at a given height. The wind stress depends on the wind speed but also on the stability of the atmospheric boundary layer, i.e. the air-sea temperature difference. The approach is based on the simple functional dependence,

$$\sigma_o = \begin{cases} \alpha(u_* - u_*^o)^\beta & if, \quad u_* > u_*^o \\ 0 & if, \quad u_* \leq u_*^o, \end{cases} \tag{6}$$

where $u_* = \sqrt{\rho_a \tau}$ is the friction velocity and ρ_a the density of air. In addition to Askari et al. [6], we have introduced a threshold u_*^o of the friction velocity, below which no surface ripples develop. The coefficients α and β depend on the parameters of radar frequency and polarisation, which are fixed for the SAR of ERS-1, and on the incidence angle ϑ and wind direction ϕ relative to the radar.

We apply Eq. (6) for investigating the influence of SST variability on the radar cross section. By making use of the atmospheric boundary layer theory (Annex B), the coefficients α and β may be determined from the σ_o-models, introduced in Section 2.1. Given different wind speeds U at the reference height of 10 m and assuming neutral stratification, i.e. $T_w = T_a$, the respective friction velocities u_* are calculated by the formula in Annex B. By varying the coefficients (α, β) within certain boundaries the σ_o values from Eq. (6) are least-squares fitted against those obtained from a σ_o-model, e.g. CMOD4. It has been found that this procedure yields well-defined *minima* in the two-dimensional parameter space.

The coefficients (α, β) have to be computed separately for different ϑ and ϕ. For the IFREMER model best fits are obtained with $u_*^o = 0$ and for CMOD4 with $u_*^o = 0.03$ ms^{-1}, which corresponds to a wind speed of 1.2 ms^{-1} for neutral stratification. At the center incident angle of $\vartheta = 23^o$ and with the wind blowing towards the satellite, ($\phi = 0$), the least-squares fit with CMOD4 data yields,

$$\alpha = 1.10, \quad \beta = 0.68, \quad u_*^o = 0.03 ms^{-1}. \tag{7}$$

Figure 4 displays the dependence of the radar cross section on the air-sea temperature difference for different wind speeds. The curves have been obtained by computing u_* as function of $T_a - T_w$ (Annex B) and σ_o by means of Eqs. (6)-(7). The diamonds represent the σ_o values of the CMOD4 model, which refers to neutral stratification. From Fig. 4 it may be concluded that in general, there is only little influence of atmospheric stability on the radar cross section, with exception in the case of very low wind speeds (below some 5 ms^{-1}) coincident with stable stratisfication ($T_a > T_w$). In these special conditions it may be expected that thermal fronts are visible in SAR images.
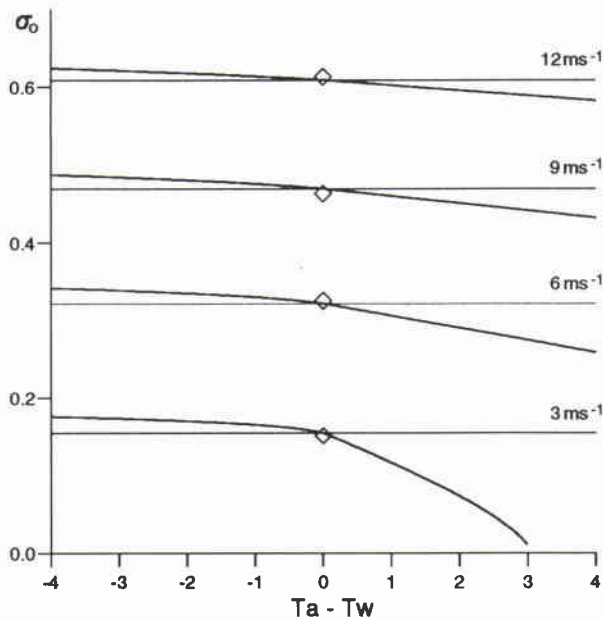

Figure 4: *Radar cross section σ_o as function of the air-sea temperature difference $T_a - T_w$ for wind speeds 3, 6, 9, and 12 ms^{-1} at the reference height of 10 m. The diamonds refer to σ_o, as determined by the scatterometer model CMOD4. The radar incidence angle is $\vartheta = 23°$ and the wind blowing towards the radar ($\phi = 0$).*

The crucial limitation of the theory is that it requires homogeneity of wind field and air temperature across the SST front. Askari *et al.* [6] report on airborne measurements with X-band (9.43 GHz) real aperture radar (RAR) at 45° incidence angle over strong SST fronts ($\Delta T \approx 6°$ C). They found variations of σ_o of the expected order but a strong dependence on wind direction and a shift of the front of σ_o against that of SST by about 3 km. They attributed these unexpected findings to heterogeneous winds in the vicinity of the front.

2.3 Surface currents

SAR images show features resembling long ocean waves (swell), internal waves and bottom topography in shallow water. Assuming that Bragg scattering is the dominant imaging mechanism, the features mentioned have to modify the short-wave spectrum in Eq. (3), most likely through the associated currents. This may happen in two different ways. First, inhomogeneities of the surface current may directly modulate the short waves. By making use of the theory of hydrodynamic modulation (Annex C), Alpers and Hennings [7] were able to explain the visibility of bottom structures in L-band SAR images of Seasat. This imaging mechanism is restricted to areas of shallow water, and strong currents, e.g. tides.

Alpers [8] applied the same theory to the imaging of internal waves. In order to obtain reasonable quantities for the modulation of the radar cross section a relatively high relaxation time of about 100× of the wave-period has to be chosen, for both bottom topography and internal waves. When applied to C-band SAR of ERS-1, which operates at shorter wavelengths than the Seasat SAR, the theory is not able to explain the observed modulation. For this reason, Lyzenga [9] suggests a second mechanism. Surface waves, which are long compared to the Bragg wavelength but not resolved by the SAR, are modulated by the underlying current, and in turn influence the radar cross section by modifying the imaging equation (electromagnetic modulation). Again, the wave-current interaction may be described by the theory of hydrodynamic modulation.

First-order modulation

Radar backscattering caused by waves propagating parallel or antiparallel to the ground projection of the radar beam, which is assumed to coincide with the x-axis, cf. Eq. (1). We describe the spatial variability of the radar-cross section by its deviation σ_1 from the mean σ_o, which are both related to the wave spectrum by Eq. (3),

$$\frac{\sigma_1(x)}{\sigma_o} = \frac{F_1(x)}{F_o}. \tag{8}$$

The spectra refer to the resonant wavenumbers as given in Eq. (1). The theory of hydrodynamicc modulation (Annex C) allows the calculation of F_1/F_o by perturbation expansion. By applying the result to waves propagating parallel or antiparallel to the x-axis, i.e. $k_x = \pm k$, $k_y = 0$, we obtain from Eq. (C7),

$$\left(\left(\frac{k_x}{k}v_g + u_{ox}\right)\frac{\partial}{\partial x} + \mu\right)F_1 = -[(\gamma_v + \gamma_x)\frac{\partial u_x}{\partial x} + \gamma_y\frac{\partial u_x}{\partial y}]F_o, \tag{9}$$

$$with, \ \ \gamma_v = \frac{k}{\omega}\frac{d\omega}{dk}, \ \ \gamma_x = -\frac{k_x}{F_o}\frac{\partial F_o}{\partial k_x}, \ \ \gamma_y = -\frac{k_x}{F_o}\frac{\partial F_o}{\partial k_y},$$

with γ_v being determined by the dispersion relation, Eq. (2). If the short-wave spectrum is isotropic in direction and decaying by $\mid \mathbf{k} \mid^{-4}$, then $\gamma_x = 4$ and $\gamma_y = 0$. Most of the results in the literature are based on this assumption. By extending the model spectrum, Eq. (5), to any two-dimensional wave vector, i.e. $F_o(\mathbf{k}) = k^{-6}(k_x \cos\phi - k_y \sin\phi)^2$, one obtains, $\gamma_x = 4$ and $\gamma_y = 2\tan\phi$. More realistic values may be obtained from the empirical σ_o-models introduced before, which by Eq. (3) determine the scattering spectrum,

$$F_o = \frac{\sigma_o(U, \phi, \vartheta)}{T(\vartheta)}. \tag{10}$$

The σ_o-models are tuned with data of the scatterometer, which illuminates areas of some 25 km in diameter. Thus, it can be assumed that the respective spectrum is of zero order, though it contains some up-downwind asymetry, which in our approach is a first-order effect. Table 3 presents values of γ_x and γ_y, which have been determined numerically by using the IFREMER σ_o-model (Annex A). Because of its non-continuous dependence on ϑ (Fig. 3) CMOD4 is not suitable for such calculations.

	$U = 3 \text{ ms}^{-1}$				$U = 9 \text{ ms}^{-1}$			
	$\vartheta = 20°$		$\vartheta = 26°$		$\vartheta = 20°$		$\vartheta = 26°$	
ϕ	γ_x	γ_y	γ_x	γ_y	γ_x	γ_y	γ_x	γ_y
$0°$	6.09	0.0	6.55	0.0	5.20	0.0	5.57	0.0
$\pm45°$	6.28	∓0.11	6.78	∓0.22	5.50	∓0.33	5.88	∓0.52
$\pm90°$	6.51	±0.05	7.08	±0.04	5.95	±0.03	6.43	±0.02
$\pm135°$	6.33	±0.16	6.85	±0.26	5.55	±0.35	5.95	±0.53
$180°$	6.17	0.0	6.65	0.0	5.27	0.0	5.65	0.0

Table 3 *Coefficients γ_x and γ_y for different wind speeds U and directions ϕ at two incidence angles ϑ, derived from the IFREMER σ_o-model.*

The relaxation rate μ, as determined by Eqs. (C8)-(C9), is strongly dependent on wind speed. Its inverse value, i.e. the relaxation time, ranges from 44× the wave period of the scattering surface waves at 3 ms^{-1} wind speed to 9× at 9 ms^{-1}.

Second-order modulation

The mechanism suggested by Lyzenga [9] considers the modulation of wind waves of a few metres wavelength by underlying currents, which in turn influence the radar cross section. Radar backscatter is caused by ripples on the longer waves which locally can be described by sloping facets. The mean radar cross section is obtained by averaging over all facets within the illuminated area. The radar cross section is

modulated not only by the facet slopes but also by associated orbital motions,

$$\sigma(\mathbf{n}) = \sigma_o(\mathbf{n})(1 + \frac{F_1}{F_o}), \tag{11}$$

where $\mathbf{n}$ is the slope vector and F_1/F_o the contribution of the orbital motion, which may be estimated by the theory of hydrodynamic modulation, i.e. perturbation methods (Annex C). Following Hasselmann [10], we expand Eq. (11) into a Taylor series around the mean slope, which is zero. Assuming that the slope angles are small and uncorrelated, and accounting for vanishing $\partial\sigma_o/\partial n_y$ (Table 4) we obtain,

$$\sigma = \sigma_o + \frac{1}{F_o}\frac{\partial\sigma_o}{\partial n_x} < F_1 n_x > + \frac{1}{2}\frac{\partial^2\sigma_o}{\partial n_x^2} < n_x^2 > + \frac{1}{2}\frac{\partial^2\sigma_o}{\partial n_y^2} < n_y^2 > +..., \tag{12}$$

where the angle brackets denote ensemble means with respect to the long waves.

Tilted facets depolarise the backscattered signal. Valenzuela [3] presents theoretical results, which show that the transfer coefficient T in Eq. (4) depends on both slope components, parallel (n_x) and perpendicular (n_y) to the radar beam. These formulas, together with a model spectrum, e.g. Eq. (5), allow estimation of the derivatives of σ_o in Eq. (12). Instead, we estimate the derivatives with aid of the IFREMER σ_o-model. The resultant incidence angle at the facet is,

$$\vartheta = \cos^{-1}[\cos(\vartheta_o - n_x)\cos n_y], \tag{13}$$

with ϑ_o being the incidence angle at the undisturbed surface. By making use of Eq. (13), first- and second-order derivatives of σ_o have been derived numerically with respect to the slope angles (Table 4).

	$U = 3\ \mathrm{ms}^{-1}$			$U = 9\ \mathrm{ms}^{-1}$		
ϕ	$0°$	$90°$	$180°$	$0°$	$90°$	$180°$
$\partial\sigma_o/\partial n_x$	14	15	14	12	14	12
$\partial^2\sigma_o/\partial n_x^2$	227	260	233	166	217	170
$\partial\sigma_o/\partial n_y$	0	0	0	0	0	0
$\partial^2\sigma_o/\partial n_y^2$	-27	-30	-28	-23	-27	-21

Table 4: *Derivatives of σ_o with respect to the tilt angles of facet slopes at the incidence angle of $\vartheta = 23°$, derived from the σ_o-model of IFREMER.*

A more detailed evaluation of the modulation terms in Eq. (13), including other effects like range modulation, is given in [11,12]. These investigations confirm that our approach includes the most important contributions. Considering comparable variances of both slope components, Table 4 shows that the long waves travelling across the radar beam contribute by an-order-of magnitude less to the σ_o-modulation than the waves travelling along the radar beam.

The modulating wind waves may be described by a Fourier presentation,

$$\zeta = \sum_{\mathbf{K}} Z_{\mathbf{K}} \exp\{i(\mathbf{Kx} - \Omega t)\} + c.c., \quad n_\alpha = \frac{\partial \zeta}{\partial x_\alpha}, \quad \frac{\partial u_\alpha}{\partial t} = -g\frac{\partial \zeta}{\partial x_\alpha}, \quad (14)$$

with ζ, n_α and u_α being the wave height and the horizontal components of slope and orbital velocity, respectively. The complex conjugate $c.c.$ has been added in order to obtain real ζ. The modulus of the wave vector $\mathbf{K}$ and the circular frequency Ω are connected by the dispersion relation of deep-water gravity waves, i.e. Eq. (2) with $\kappa = 0$. The wind waves are assumed to be a random homogeneous process with,

$$< Z_{\mathbf{K}} >= 0, \quad < Z_{\mathbf{K}} Z_{\mathbf{K}'} >= 0 \ if, \quad Z_{\mathbf{K}'} \neq Z_{\mathbf{K}}^*. \quad (15)$$

The spectral perturbation F_1 is determined by Eq. (C6). The right-hand side of the equation may be evaluated as in Eq. (9). In accordance with Table 3, we neglect γ_y against γ_x,

$$\left(\frac{\partial}{\partial t} + \mu\right) F_1 = -(\gamma_v + \gamma_x)\frac{\partial u_x}{\partial x} F_o. \quad (16)$$

By making use of Eqs. (14)-(15) the solution becomes,

$$F_1 = F_o \sum_{\mathbf{K}} R_x Z_{\mathbf{K}} \exp\{i(\mathbf{Kx} - \Omega t)\} + c.c., \quad R_x = \frac{\Omega(\gamma_v + \gamma_x)}{K(\Omega + i\mu)} K_x^2. \quad (17)$$

Inserting the slope, Eq. (14), and the spectral perturbation, Eq. (17), into Eq. (13), taking into account the statistical properties, Eq. (15), and replacing the summation by an integration with, $< Z_{\mathbf{K}} Z_{\mathbf{K}}^* >= 1/2 E(\mathbf{K}) d\mathbf{K}$, one obtains,

$$\sigma = \sigma_o + \int_{\mathbf{K}} \left(Im(K_x R_x)\frac{\partial \sigma_o}{\partial n_x} + \frac{K_x^2}{2}\frac{\partial^2 \sigma_o}{\partial n_x^2} + \frac{K_y^2}{2}\frac{\partial^2 \sigma_o}{\partial n_y^2}\right) E(\mathbf{K}) d\mathbf{K}. \quad (18)$$

For numerical investigations, a Pierson-Moskowitz [13] spectrum is considered with a $\cos^4$-directional distribution,

$$E(\mathbf{K}) = \begin{cases} 0.0035 K^{-4} \exp[-0.74(\Omega/(KU))^4] \cos^4(\varphi - \phi), \\ 0 \ if, \ |\varphi - \phi| > \pi/2, \end{cases} \quad (19)$$

$$with, \quad \varphi = \pi - tan^{-1}(K_y/K_x),$$

with U being the mean wind speed and ϕ the wind direction with respect to the satellite (Fig. 1). The angular distribution of the long waves is assumed to be narrower than that of the short Bragg waves represented by Eq. (5).

Numerical values of the three modulating terms in the right-hand side of Eq. (18) are listed in Table 5. The integration has been carried out over wavelengths from 0.5 m to 20 m, where the lower bound is an order of magnitude above the Bragg wavelength and the upper bound about the resolution of the SAR. The extension

of the interval to smaller waves mainly effects $\sigma_{x,y}/\sigma_o$, and the extension to longer waves σ_c/σ_o, in both cases by an increase of up to 50%.

		U = 3 ms^{-1}			U = 9 ms^{-1}		
	ϕ	0°	90°	180°	0°	90°	180°
$\vartheta = 20^0$: σ_c/σ_o		0.01	0.00	-0.01	0.10	0.00	-0.10
σ_x/σ_o		1.12	0.25	1.15	1.28	0.33	1.31
σ_y/σ_o		-0.04	-0.19	-0.04	-0.05	-0.27	-0.05
$\vartheta = 23°$: σ_c/σ_o		0.01	0.00	-0.01	0.11	0.00	-0.11
σ_x/σ_o		0.90	0.21	0.93	1.03	0.27	1.06
σ_y/σ_o		-0.02	-0.12	-0.02	-0.03	-0.17	-0.03
$\vartheta = 26°$: σ_c/σ_o		0.01	0.00	-0.02	0.11	0.00	-0.11
σ_x/σ_o		0.72	0.17	0.75	0.83	0.22	0.85
σ_y/σ_o		-0.02	-0.10	-0.02	-0.02	-0.14	-0.02

Table 5: *Modulation of the radar cross section due to wind waves at different incidence angles ϑ. The quantities σ_c, σ_x, and σ_y refer to the three terms in Eq. (18), i.e. modulation by orbital motions and both components of slopes, respectively. The Pierson-Moskowitz spectrum, Eq. (19), has been used with wavelengths covering the range from 0.5 m to 20 m.*

The effect of underlying currents on the wind-sea spectrum may by estimated by means of the action balance equation, Eq. (C7), which, after some modification, reads,

$$\left((V_{g\alpha} + u_{o\alpha})\frac{\partial}{\partial x_\alpha} + \mu\right)E_1(\mathbf{K}, \mathbf{x}) = K_\beta \frac{\partial u_\beta}{\partial x_\alpha}\left(\frac{1}{E_o}\frac{\partial E_o}{\partial K_\alpha} - \frac{V_{g\alpha}}{\Omega}\right)E_o(\mathbf{K}), \quad (20)$$

where $V_{g\alpha} = \partial\Omega/\partial K_\alpha$ is the group velocity. For numerical investigations we use the parameterisation of the relaxation rate, Eq. (C8), and the Pierson-Moskowitz spectrum, Eq. (19), for E_o.

3

SAR images from coastal areas

SAR images analysed in this report are so-called precision products (SAR.PRI), which are three-look images, corrected for antenna gain elevation and range spreading loss. The spatial resolution is < 33 m in range and < 30 m in azimuth. The data represent the amplitudes of the backscattered signal and are provided with a pixel size of 12.5 m in both range and azimuth. The mid-incidence angle is $23°$ to the right from the satellite track (Fig. 1) and the image size some 100 km in both directions. The normalized radar cross section σ_o may be derived from the squared amplitudes. Pixel averaging is necessary to compensate for speckle and ensure statistical validity of the radar cross section. Following Laur [14], we derive σ_o from the SAR.PRI data p_i by,

$$\sigma_o = \frac{1}{N} \sum_{i=1}^{N} \frac{p_i^2 \sin \vartheta}{K \sin \vartheta_m}, \tag{21}$$

where K is a calibration constant provided with the data, ϑ the incidence angle and $\vartheta_m = 23°$ its value at mid-range.

In order to allow a better comparison with data from other sources, SAR images have been transformed to a north-orientated coordinate system. A grid of a given spacing, normally 200 m in both directions, has been defined and the original SAR data averaged according to Eq. (21) within the grid resolution cells.

3.1 Norwegian coastal waters

The Norwegian coastal waters are characterised by a very distinct frontal structure between the cold northward flowing coastal water of low salinity and the warmer Atlantic water of higher salinity. For this region, Johannessen et al. [2] showed that SAR imagery may express features with configurations in good agreement with those seen in an AVHRR image of sea-surface temperature. They attributed the SAR image characteristics to wave-current interaction along the current (thermal) fronts.

In the context of studying the circulation in the northern Atlantic, SACLANTCEN purchased and processed a number of 1993 AVHRR images. Searching for coincident SAR images taken under low-wind conditions, we found two dates, 14 April and 10

September 1993. While the SAR images of the first date show the expected features, those from the second date reveal no features at all, probably due to stronger winds. Figure 5 presents the location of two SAR frames from the first date, with surface winds analysed by the UK Meteorological Office, 1.5 h after the ERS-1 overpass at 10:32 UT. The wind analysis is based on a numerical prediction model, which makes use of the repeated insertion of observational increments. The winds have been taken from the lowest of 20 atmospheric levels, referring to roughly 25 m above the sea surface.
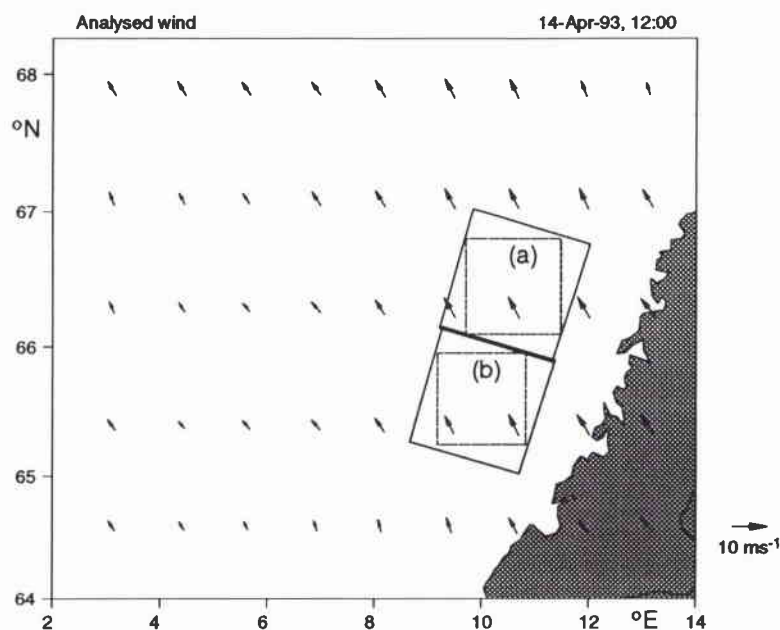
Figure 5: *SAR frames of ERS-1 in Norwegian coastal waters together with the analyzed wind field of the UK Meteorological Office, 90 min after the satellite overpass. The dashed frames refer to subsequent Figs. 6 - 7.*

North-orientated SAR images covering the two dashed frames in Fig. 5 are displayed in Fig. 6. The radar cross section as defined by Eq. (21) averaged within resolution cells of 200 × 200 m, is presented. The data will be used for comparing measured values of σ_o with those retrieved from the wind field by means of a σ_o-model. Satellite-measured brightness temperatures for the areas of the two SAR images are displayed in Fig. 7. The data are from channel-4 of the AVHRR of NOAA-11, taken 3.5 h after the SAR images. From a first examination it seems obvious that the features on the SAR images are related to the temperature structures.

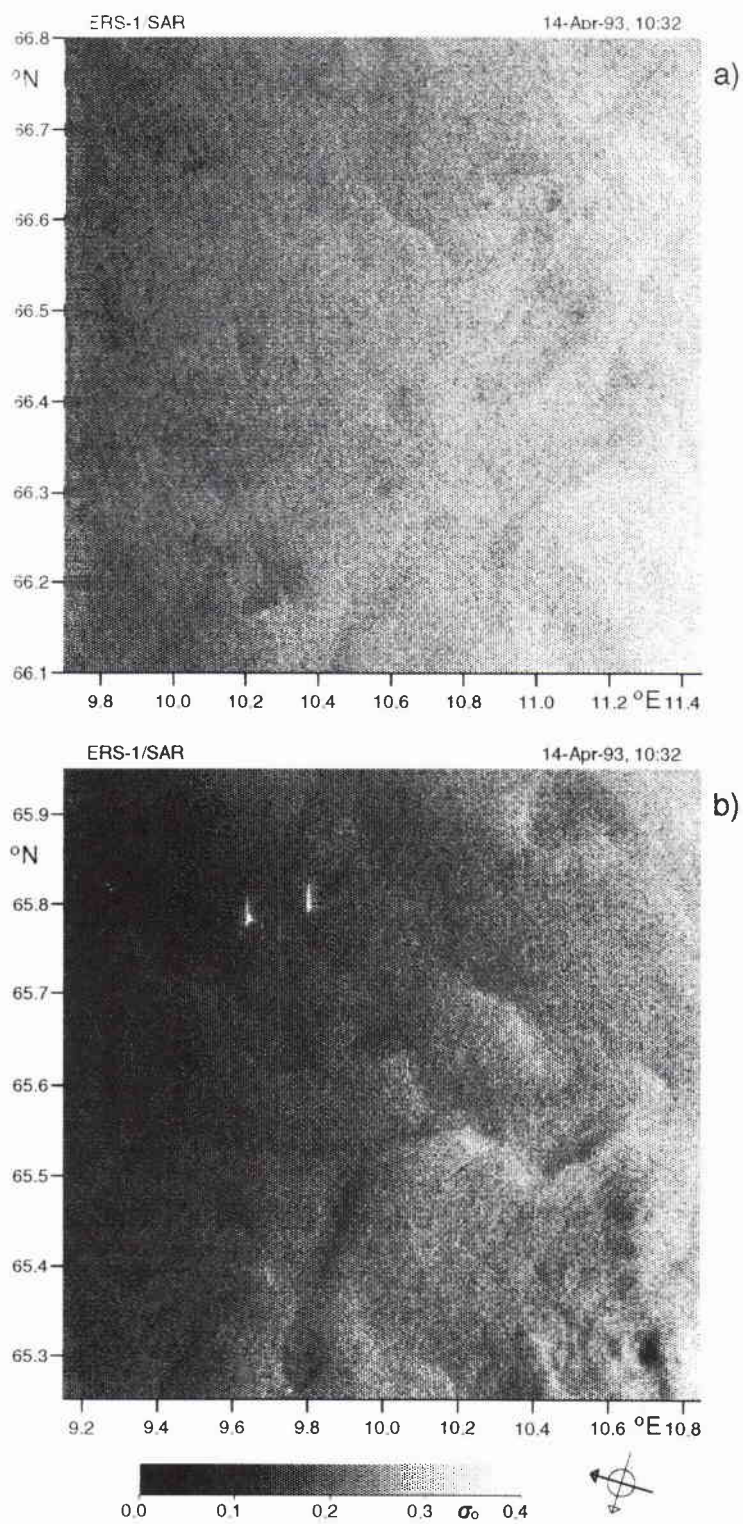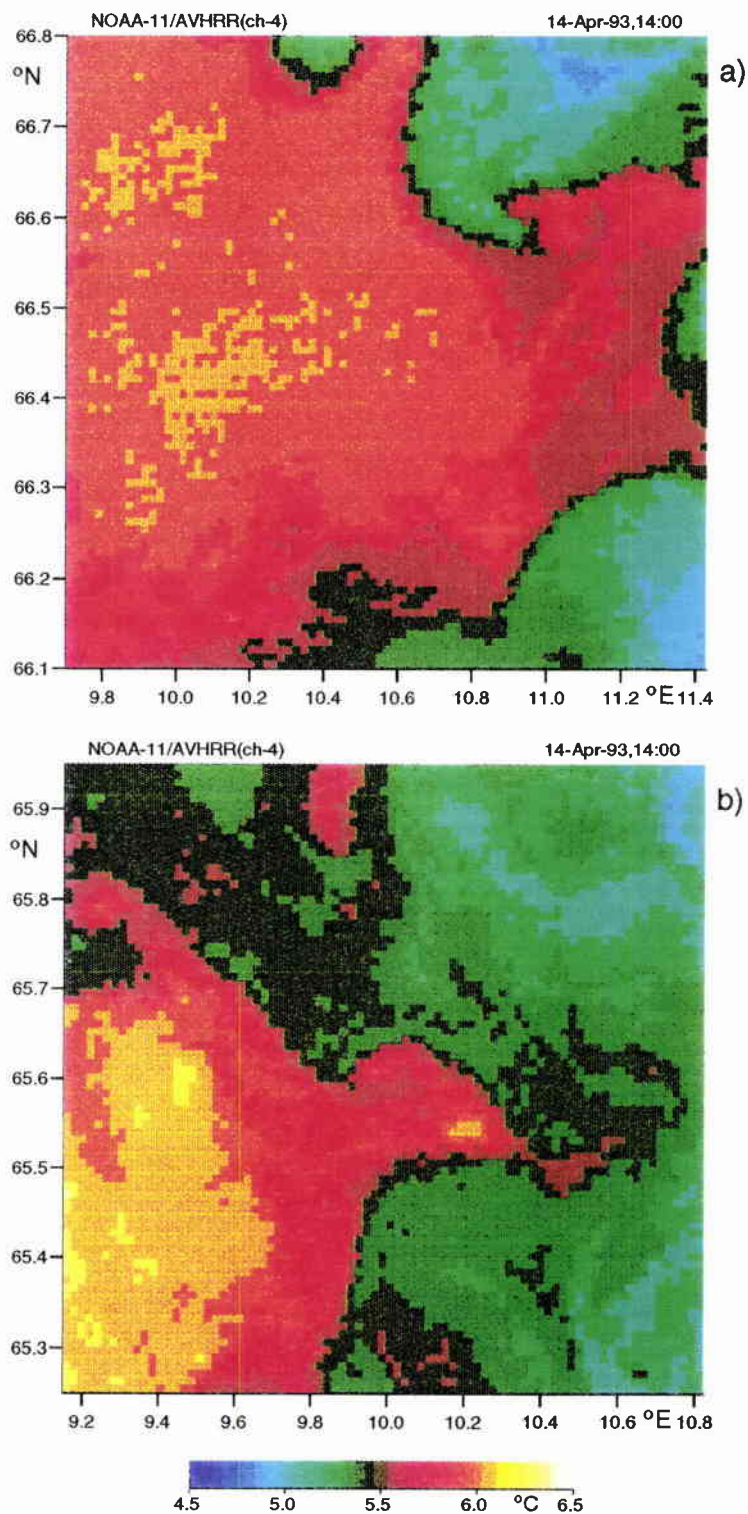**Figure 6:** *North-orientated SAR images, covering the areas indicated by the dashed frame (a) and (b) in Fig. 5.*

Figure 7: *Channel-4 brightness temperatures of the AVHRR of NOAA-11, covering the same areas as the SAR images in Fig. 6.*

3.2 Area south of Elba (Mediterranean)

The Mediterranean SAR images presented, i.e. from the Elba and Sicily area, have been acquired during cruises of NRV *Alliance*. *In situ* measurements of surface meteorological data and sea-surface temperature have been performed with the ZENO-Alliance network (ZAN), ZENO and ZAN being trade names of the Coastal Climate Company (Seattle, USA). ZAN is a monitoring system designed specially for shipboard installation [15]. The network integrates measurements of apparent wind, air temperature, relative humidity, barometric pressure and water temperature with information on ship position, course and heading.

During an acoustic experiment in late summer 1994, two SAR images were acquired, on 27 August and 2 September. Figure 8 shows the experimental area together with the bathymetry. The positions of NRV *Alliance* during the satellite overpasses are shown, the wind speeds U are given and the directions indicated.
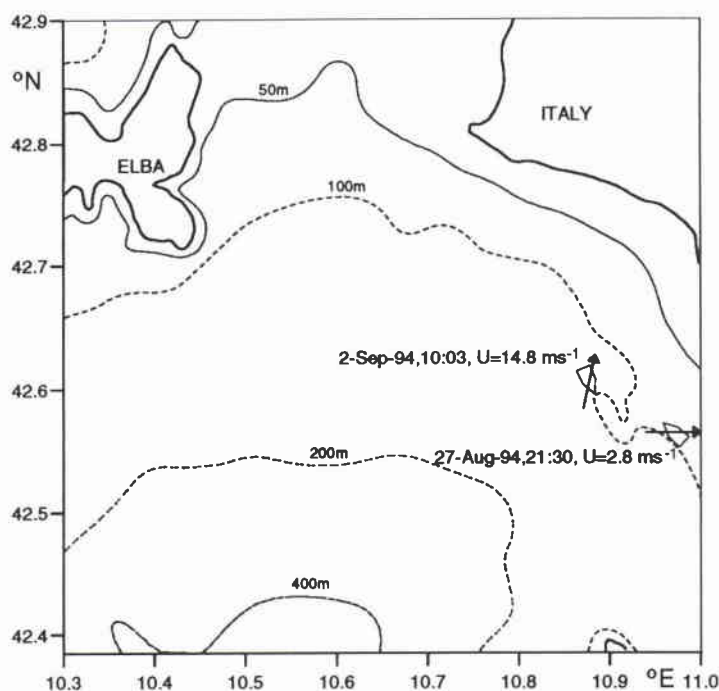

Figure 8: *Experimental area south-east of Elba with depth contours at 50, 100, 200, and 400 m. Times and wind speeds U refer to the ERS-1 overpasses. Respective locations of NRV Alliance are given and wind directions indicated by arrows.*

The SAR data from 27 August (Fig. 9) with a resolution of 200 m, cover only part of the area of Fig. 8, but just contain the position of NRV *Alliance*. Figure 10 displays 6 h time series of air- and water temperature (2 m below sea surface), wind speed and direction (16 m above sea level).
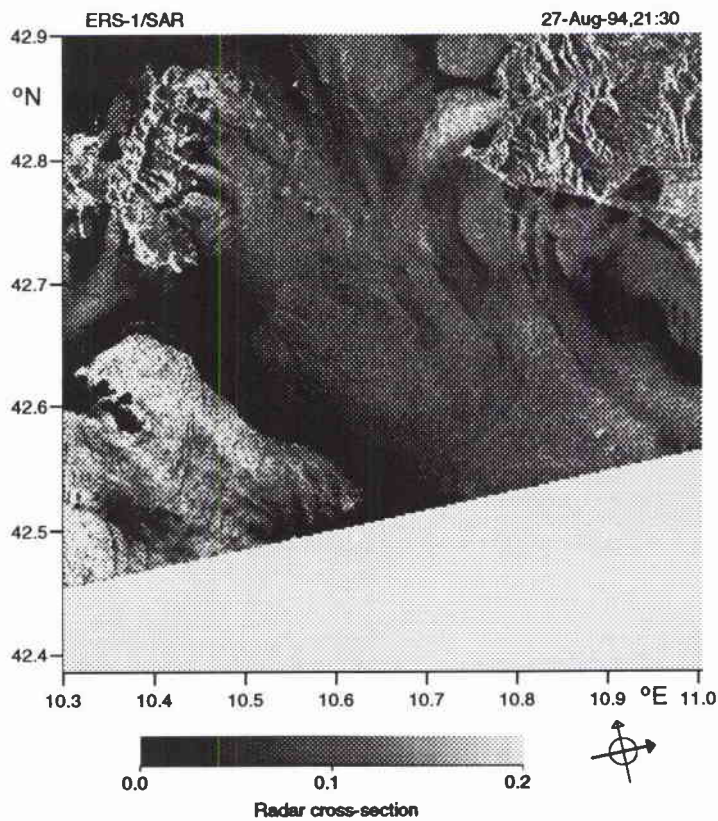
Figure 9: *North-orientated SAR image covering the area of Fig. 8. Resolution cells are 200 × 200 m.*
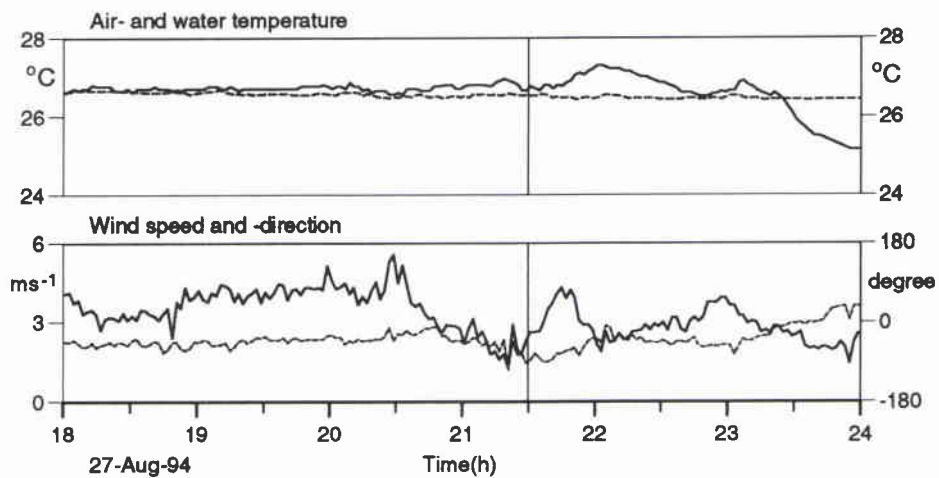

Figure 10: *Time series of meteorological parameters and sea surface temperature around the ERS-1 overpass of the Elba area on 27 August 1994, measured from onboard NRV Alliance. Vertical lines indicate the time of the satellite overpass.*

Figure 11 shows channel-4 brightness temperatures from the AVHRR of NOAA-11, taken 4.5 h earlier than the SAR image. Some features of the temperature image appear to correspond with those of the SAR image of Fig. 9.
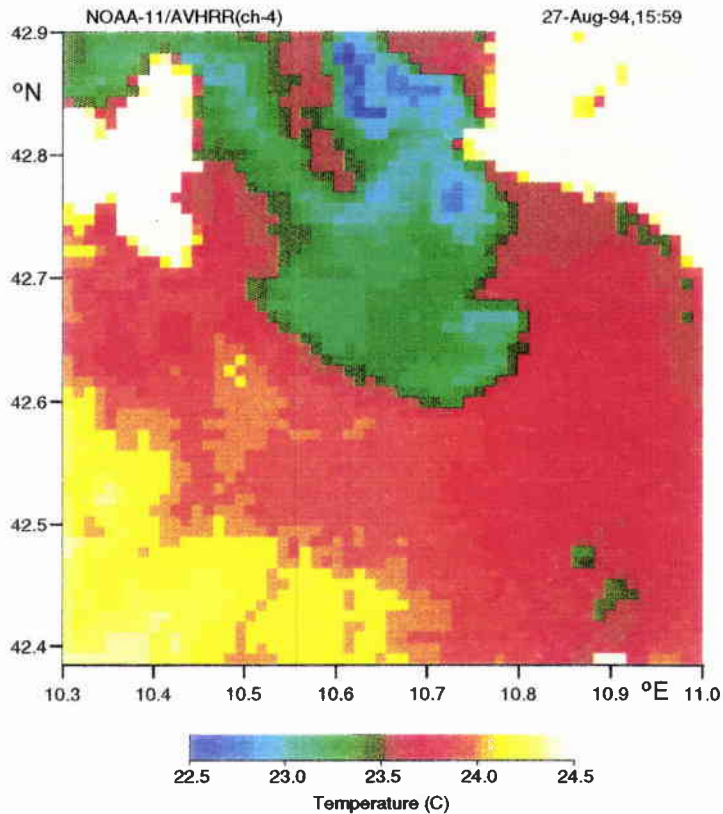

Figure 11: *Channel-4 brightness temperatures of the AVHRR of NOAA-11, covering the area of Fig. 8.*

During 2 September, winds were relatively strong and it is most likely that the features in Fig. 12 are caused by surface wind variability. Air- and water temperature, wind speed and direction from about 3 h before to 3 h after the satellite overpass are presented in Fig. 13. Because of cloud coverage, no coincident satellite measurements of sea-surface temperature are available.

The SAR images of the Elba area will be used for quantitatively investigating the dependence of σ_o on wind and the imaging of temperature fronts.
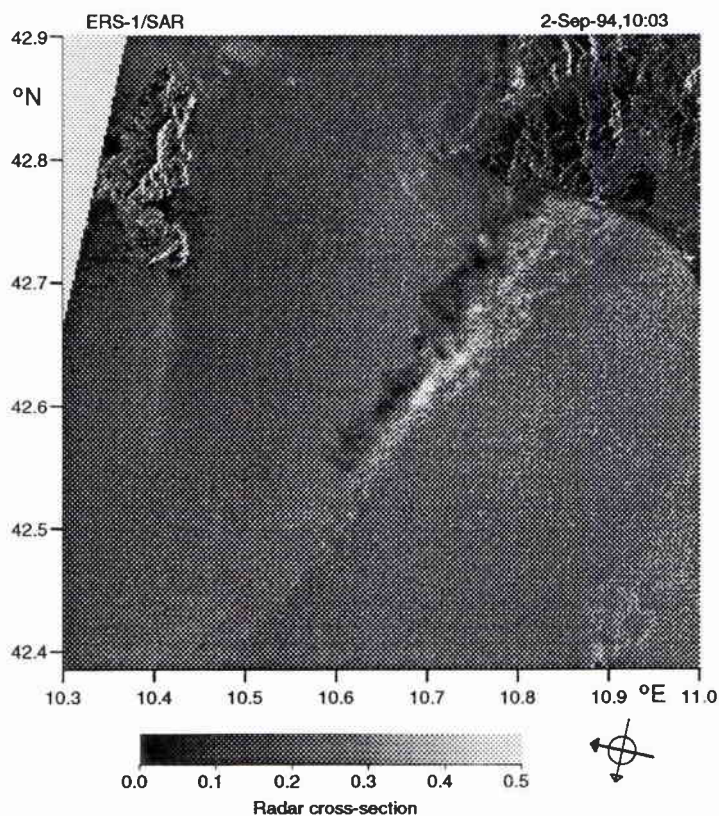
Figure 12: *North-orientated SAR image covering the area of Fig. 8. Resolution cells are 200 × 200 m.*
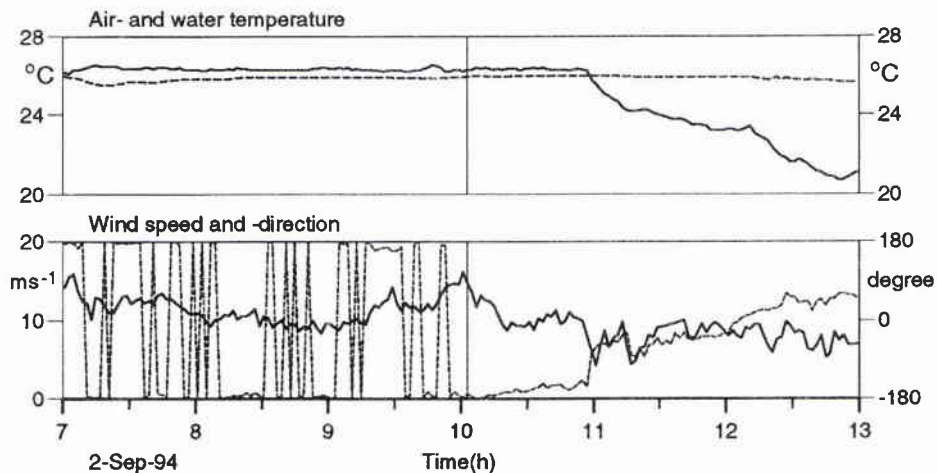

Figure 13: *Time series of meteorological parameters and sea surface temperature around the ERS-1 overpass of the Elba area on 2 September 1994, measured from onboard NRV Alliance. Vertical lines indicate the time of the satellite overpass.*

3.3   Area south of Sicily (Mediterranean)

During a hydrographic survey of the area south of Sicily in November 1994, carried out by NRV *Alliance*, SAR images from two overpasses of ERS-1 are available. For each overpass, one image has been selected for further analysis. Figure 14 shows the locations of the images and the bathymetry of the area. The respective positions of NRV *Alliance* are indicated, as well as the wind speed and direction.
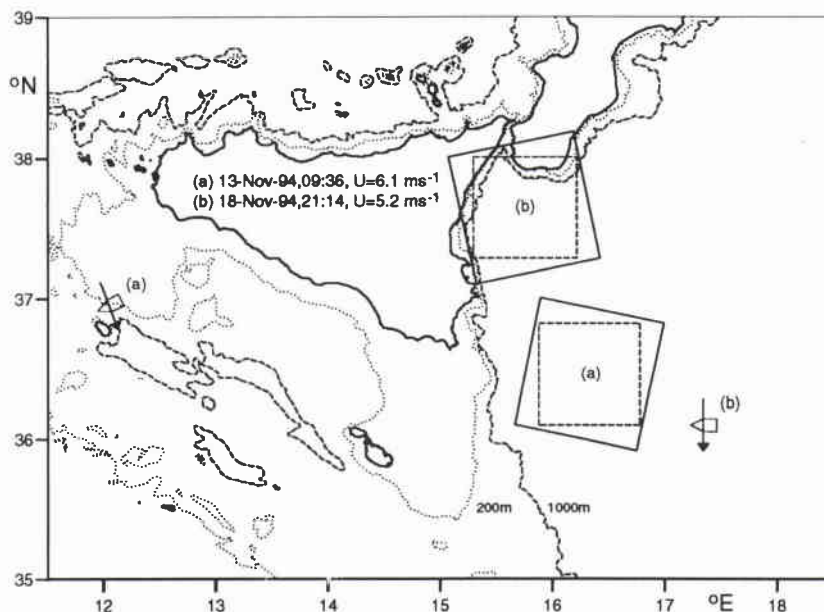

Figure 14: *Experimental area south-east of Sicily with depth contours at 200, 1000, and 2000 m. Times and wind speeds U refer to the ERS-1 overpasses. Respective locations of NRV Alliance are given and wind directions indicated by arrows.*

The two SAR images (a) and (b) are presented in Fig. 15 and Fig. 17, respectively. Figure 16 and Fig. 18 display 6 h time series of air- and water temperature (2 m below sea surface), wind speed and direction (16 m above sea level) around the satellite overpasses. Because of cloud coverage no coincident AVHRR images are available. Figure 15 reveals a light stripe in the center of the SAR image, which might be caused by a current front. Figure 17 shows wave-like structures, which are probably due to internal waves. The discussion of both figures will concentrate on the question how current variability is reproduced in SAR images and to what extent quantitative information can be derived.

Figure 15: *North-orientated SAR image, covering the area indicated by the dashed frame (a) in Fig. 14. Resolution cells are 200 × 200 m.*

Figure 16: *Time series of meteorological parameters and sea surface temperature around the ERS-1 overpass of the Sicily area on 13 November 1994, measured from onboard NRV Alliance. Vertical lines indicate the time of the satellite overpass.*
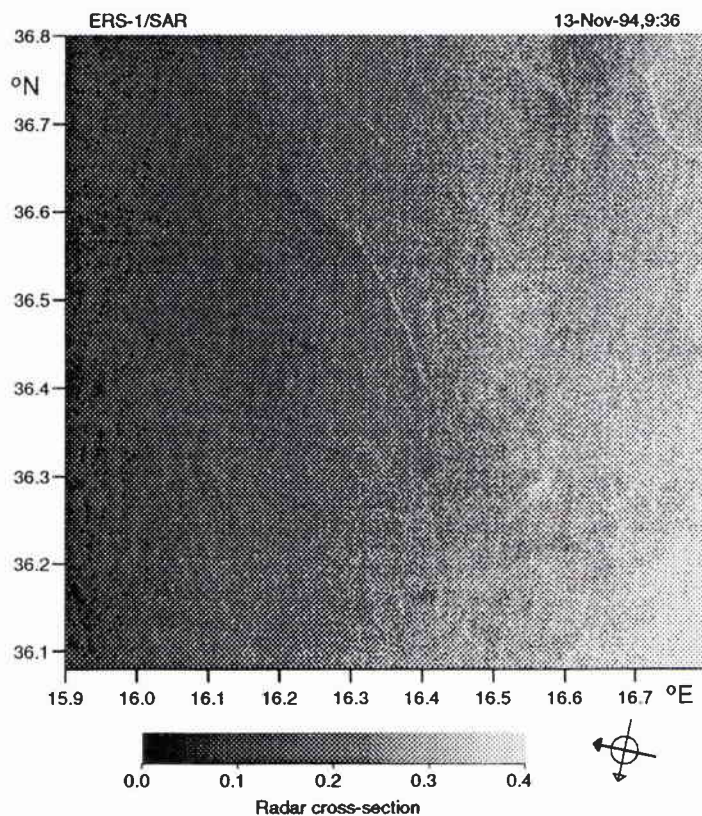
Figure 17: *North-orientated SAR image, covering the area indicated by the dashed frame (b) in Fig. 14. Resolution cells are 200 × 200 m.*
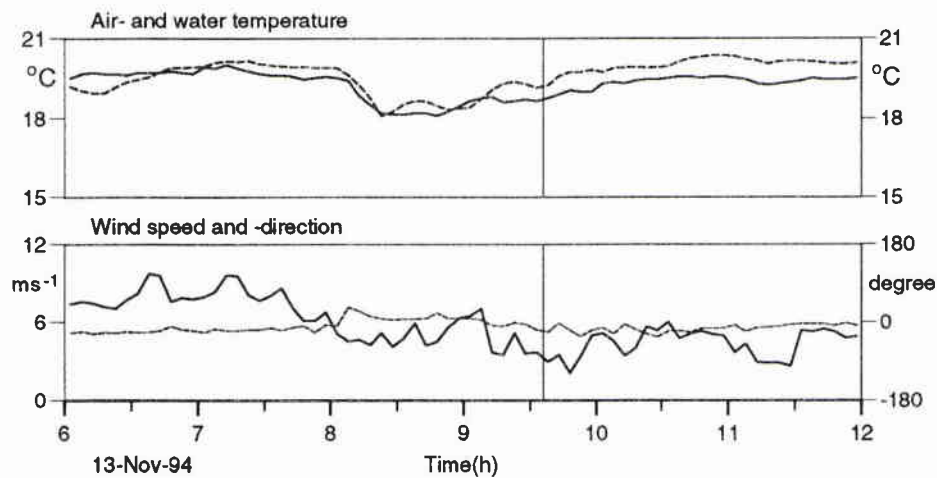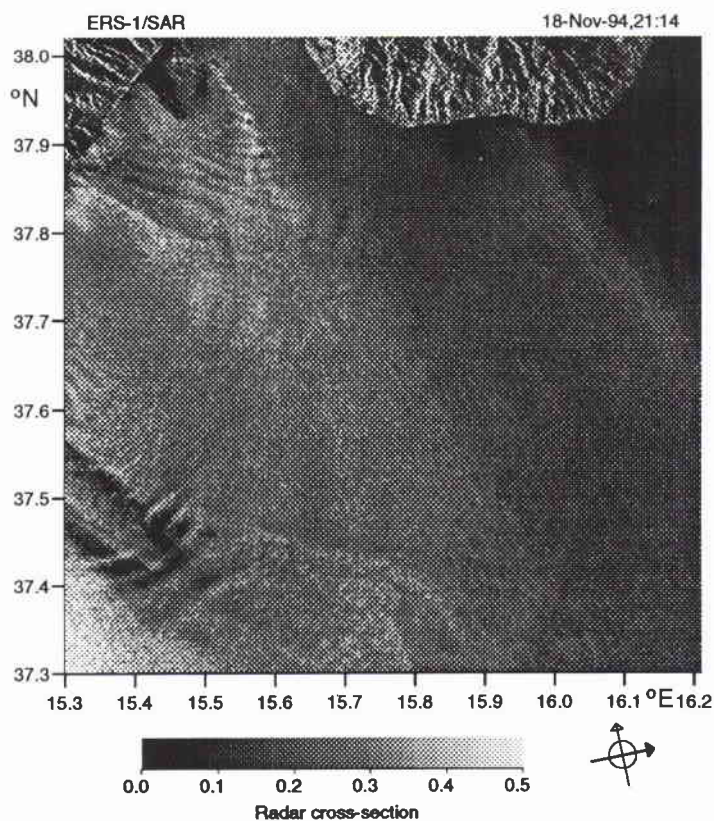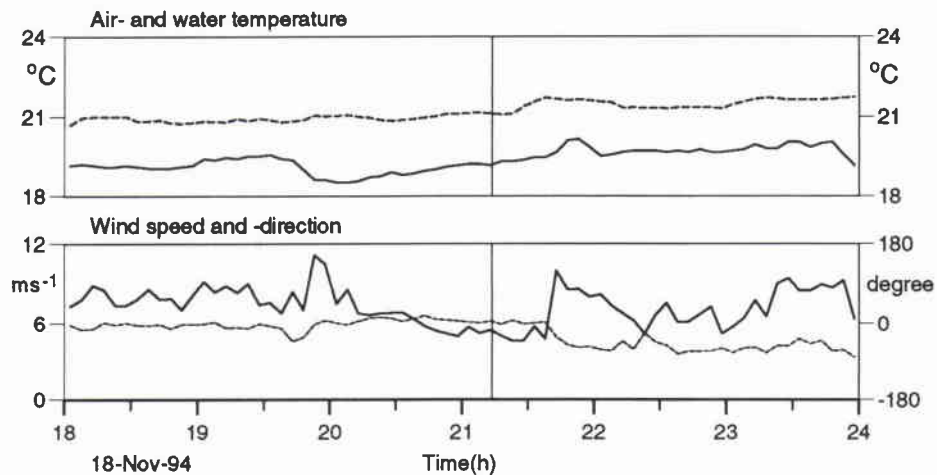

Figure 18: *Time series of meteorological parameters and sea surface temperature around the ERS-1 overpass of the Sicily area on 18 November 1994, measured from onboard NRV Alliance. Vertical lines indicate the time of the satellite overpass.*

4

Interpretation of the SAR images

In this section we use the theoretical approaches, outlined in Section 2, to extract quantitative information from the SAR images of Section 3 and compare the results with ground-truth data available.

4.1 Determination of wind speed

Reliable estimate of surface winds from the radar cross sections σ_o of a SAR image requires *a priori* knowledge of wind direction (Fig. 3). E.g., $\sigma_0 = 0.4$ may be due to a wind of 9 ms^{-1} blowing parallel or even higher than 12 ms^{-1} blowing perpendicular to the radar beam. Information on the wind direction is often available from weather charts or analyzed wind fields, such as that of the UK Meteorological Office presented for the Norwegian coast (Fig. 5).

The wind direction relative to the radar ϕ, as defined in Fig. 1, is related to the meteorological wind direction α_w and the heading of the satellite α_s by,

$$\phi = \alpha_w - \alpha_s - 90^o, \tag{22}$$

where both α_w and α_s count clockwise from north and α_w is the direction from which the wind is blowing (meteorological convention).

For the retrieval of wind speeds from SAR radar cross sections, data of different areas will be used. Figure 5 shows the location of two SAR images, which are presented in Figs. 6a-b. One section of each frame has been chosen which connects grid points of the analyzed wind field in Fig. 5. The wind direction within these four grid points is about constant, $\phi = -135^o$ relative to the radar. In order to suppress speckle noise, σ_o values have been averaged over 500×500 m resolution cells according to Eq. (21).

Figure 19 displays the σ_o values (dotted lines) and wind speeds as retrieved by two different σ_o-models (dashed and full lines). The data of the upper section refer to Fig. 6a, those of the lower section to Fig. 6b. Though the σ_o values increase along both sections, the wind speeds differ due to the incidence angle of the radar beam. The analyzed wind speeds are represented by diamonds at each end of the sections. These values agree well with the SAR-retrieved winds, except for the end

of the lower section. When comparing SAR with analyzed wind speeds it must be taken into account that the latter represent averages over large areas and several hours. The advantage of the SAR data is the possibility of analyzing the small-scale variability.
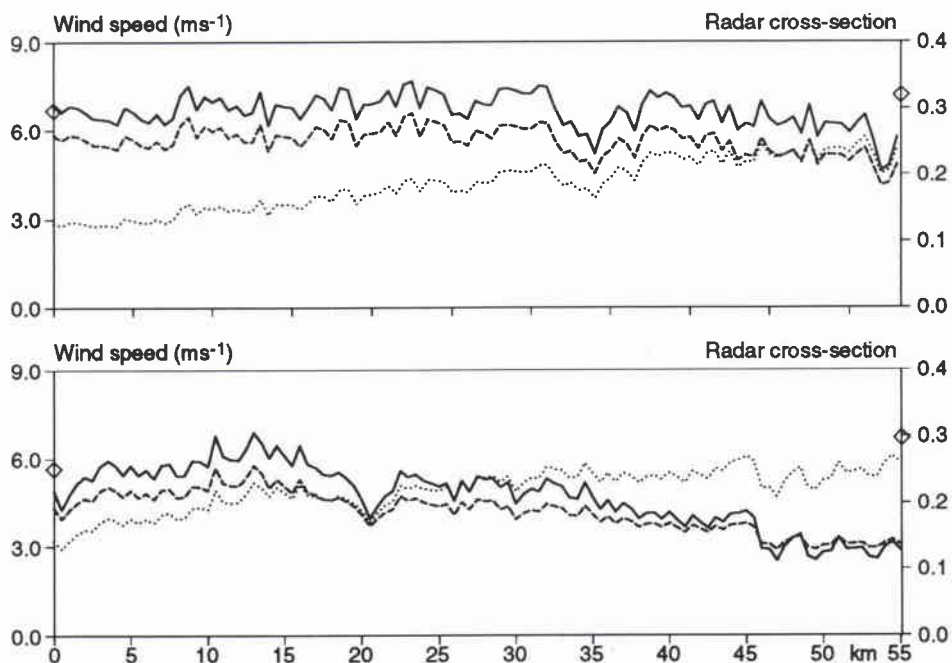

Figure 19: *Wind-speeds retrieved from SAR radar-cross sections σ_o in Norwegian coastal waters. The sections displayed connect two grid points of the analyzed wind field in Fig. 5, from 9.4°E to 10.6°E at 66.3°N (upper panel) and 65.4°N (lower panel). The analyzed wind speeds are represented by diamonds. The IFREMER σ_o-model (full lines) and CMOD4 (dashed lines) have been applied, with a wind direction of $\phi = -135°$ relative to the satellite. The σ_o values used (dotted lines) are averages within 500×500 m resolution cells.*

Ground-truth data for the two SAR images from the Elba area, taken on 27 August (Fig. 9) and 2 September 1994 (Fig. 12), have been recorded aboard NRV *Alliance*. Both SAR images cover the position of the ship (Fig. 8), but were taken under very different wind conditions (Fig. 10 and 13, respectively). While, for the time of the satellite overpass, the wind speed was very low on 27 August (≈ 3 ms^{-1}) it was high on 2 September (≈ 15 ms^{-1}).

Figure 20 displays SAR-retrieved wind speeds along west-east orientated sections of some 50 km length which end at the positions of NRV *Alliance* (Fig. 8). Wind directions are taken from the ship measurement and are about $\phi = -170°$ (27 August) and $\phi = -90°$ (2 September). It should be mentioned that the assumption of constant wind direction along the whole sections may be wrong and a cause of

error, especially for higher wind speeds (Fig. 3). By chance, the wind direction on 2 September yields maximum values for the retrieved speeds, i.e. a change of wind direction along the section would introduce lower wind speeds.
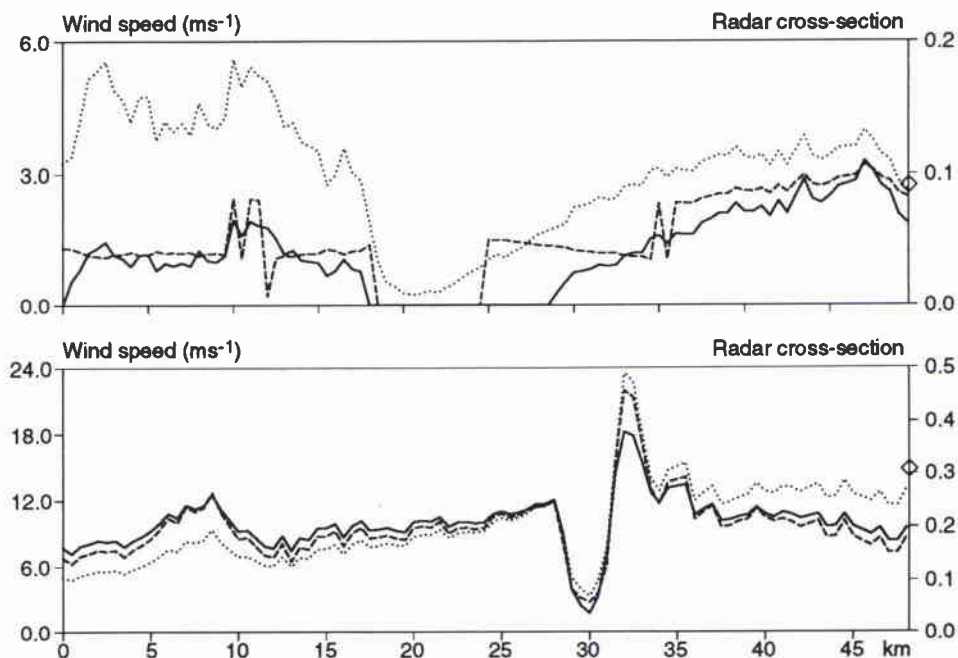

Figure 20: *Wind-speeds retrieved from SAR radar-cross sections σ_o south of Elba. The sections end at the position of NRV Alliance (Fig. 8) and are from 10.37°E to 10.97°E at 42.56°N (upper panel) and from 10.29°E to 10.89°E at 42.61°N (lower panel). Ship-measured wind speeds are represented by diamonds. For retrieval, the σ_o-models of IFREMER (full lines) and CMOD4 (dashed lines) have been applied, with wind directions relative to the satellite of $\phi = -170°$ and $-90°$, respectively. The σ_o values used (thin dotted lines) used are averages within 500×500 m resolution cells.*

The main features in Fig. 9 (27 August) are due to the variability of the low-speed wind field. The ship measurements (Fig. 10) reveal values between 2 and 4 ms^{-1}. In this range, σ_o is very sensitive to slight changes of wind speed and decreases to nearly zero below a certain threshold, when no surface-ripples are generated. The upper panel of Fig. 20 shows excellent agreement of the measured wind speed (diamond at the end of the section) with those retrieved from the SAR image.

The features in the SAR image of Fig. 12 (2 September) are probably due to meteorological conditions. The ship measurements (Fig. 13) show that a strong gust of wind passed the ship when the SAR image was taken. The SAR image also indicates the presence of a gust but some 10 km north-west of the position of the ship. The satellite-retrieved wind speed at the position of the ship is 9 ms^{-1}, i.e. considerably

lower than the real wind speed of 15 ms^{-1}, represented by the diamond in the lower panel of Fig. 20. The probable explanation for this discrepancy is rainfall during the satellite overpass. The ship's log reports the passage of a thunderstorm, which might have caused the conspicuous features in Fig. 12. The lower panel of Fig. 20 reveals that σ_o changes from less than 0.1 to nearly 0.5 within only 2 km. It is probable that the varying rainfall density strongly influences the σ_o distribution. It should be also mentioned that the maximum wind speeds, as retrieved by the two σ_o-models, differ considerably.

4.2 Imaging of temperature fronts

Changes in SST cause changes in the surface wind stress, which in turn influence the radar cross section. When the wind field and the air temperature are homogeneous, the theory presented in Section 2.2 predicts the degree of change depending on wind speed and air-sea temperature difference. It is stronger for stable than unstable stratification and decreases with increasing wind speed. Higher SST causes higher σ_o.

If available, satellite images of SST (retrieved from the AVHRR) are presented with the SAR images in Section 3. When comparing AVHRR and SAR data it must be taken into consideration that they are separated by several hours, during which the sea conditions may have changed. Accuracy is affected by positioning errors of the order of 1 km, estimated from imaged coastlines and satellite sensor (AVHRR) resolution.

From corresponding SAR and AVHRR images, three sections of 30 km length were chosen. Along these sections, Figures 21-23 compare values of σ_o with the channel-4 brightness temperature, which in general underestimates the SST by a few degrees. Two of the figures refer to data from Norwegian coastal waters and one to the area south of Elba. The resolution of the AVHRR depends on the vertical look angle of the AVHRR, which is about 1.2 km for the examples presented. In order to suppress most of the speckle noise, averages of σ_o within 500 × 500 m resolution cells are displayed. The dependence of σ_o on the incidence angle ϑ may introduce a trend, especially if this is orientated parallel to the radar beam. A corrected value σ_c (dotted lines) is presented with the measured σ_o (dashed lines), which is more appropriate for comparison with SST and defined by,

$$\sigma_c = \left(\frac{\sin \vartheta}{\sin \vartheta_m}\right)^4 \sigma_o, \qquad (23)$$

where $\vartheta_m = 23^o$ is the mid-range incidence angle. As may be concluded by comparing Figs. 2 and 3 this is a reasonable correction for wind speeds in the range 3 - 6 ms^{-1}.

Figure 21 presents sections through the SAR and AVHRR images of Fig. 6a and Fig. 7a, respectively. The sections cross significant features within the SAR image, a broader dark band (upper panel) a sharp edge separating light and dark areas (middle panel) and a dark area of some 2 km in diameter (lower panel). In contrast to the theory, the upper panel reveals decreasing σ_o in an area of increasing SST.

Figure 21: *Comparison of radar-cross sections (dashed lines) and brightness temperatures (full lines) along three 30 km sections in Norwegian coastal waters, extracted from Figs. 6a and 7a. Starting point and orientation are indicated. The σ_o values are means within 500×500 m resolution cells. Values corrected by Eq. (23) for 23° incidence angle (dotted lines).*

The lower panels contain sharp σ_o decreases, which correspond to SST fall-offs shifted by some 2 km. This shift may be due to inaccuracy in positioning or a northward flowing current of 0.2 ms^{-1}, which displaced the SST features during the 3.5 h period between SAR and AVHRR images. The degree of change in σ_o is

higher than predicted by theory. In addition, σ_o shows variations of the same order, unrelated to SST variability.

Figure 22 presents sections through the SAR and AVHRR images of Fig. 6b and Fig. 7b. The upper two panels reveal sections which pass through the warm water cell in the central part of Fig. 7b from south to north or west to east, respectively.
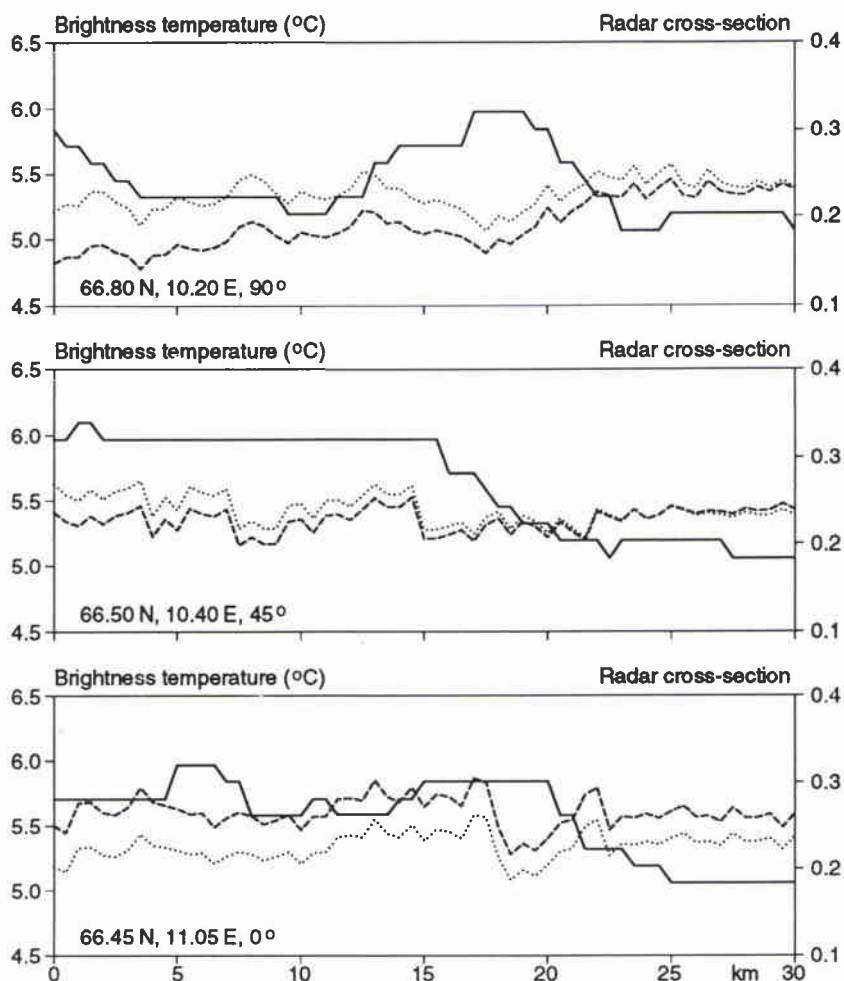

Figure 22: *Comparison of radar-cross sections (dashed lines) and brightness temperatures (full lines) along three 30 km sections in Norwegian coastal waters, extracted from Figs. 6b and 7b. Starting point and orientation are indicated. The σ_o values are means within 500 × 500 m resolution cells. Values corrected by Eq. (23) for 23° incidence angle (dotted lines).*

As expected, an increase of SST is accompanied by an increase of σ_o. Again, the shift between the fronts of about 2 km in the upper panel may be caused by a northward flowing current. The incidence angle of the SAR at the warm water cell

is $\vartheta = 22.1°$ and the mean wind direction with respect to the satellite, $\phi = -135°$. The lower panel of Fig. 22 displays a section with considerable changes in σ_o but nearly constant SST.

By applying the theory of Section 2.2, Table 6 predicts σ_o values for the maximum air-sea temperature difference of the data in Fig. 22 and two different wind speeds. It has been assumed that the air temperature is the same as the SST at the warmer side of the front.

σ_o-model	U	$T_a - T_{w1}$	$T_a - T_{w2}$	σ_{o1}	$\Delta\sigma_o$
CMOD4	5.0 ms^{-1}	0.0°C	0.8°C	0.289	-0.014
IFREMER	5.0 ms^{-1}	0.0°C	0.8°C	0.256	-0.012
CMOD4	4.0 ms^{-1}	0.0°C	0.8°C	0.238	-0.020
IFREMER	4.0 ms^{-1}	0.0°C	0.8°C	0.213	-0.016

Table 6: *Theoretically predicted differences of the radar cross-section $\Delta\sigma_o = \sigma_{o2} - \sigma_{o1}$ across a temperature front $\Delta T = T_{w2} - T_{w1}$ for two different wind speeds. The computations refer to the data from Norwegian coastal waters, presented in Fig. 22.*

The tuning of Eq. (6) by the two σ_o-models leads to higher σ_o values and differences for CMOD4 compared with the IFREMER model. The values are of the order of those measured along the two sections (upper panels of Fig. 22), but the differences are too small by at least a factor 2. An increase of the air-sea temperature differences by a constant amount has almost no influence on the results. A decrease however, leads to unstable atmospheric stratification and smaller differences in σ_o.

The comparison of Fig. 9 and Fig. 11 from the Elba area, reveals that most of the σ_o variability is not related to SST changes. This is also obvious along the three sections in Fig. 23. However, the upper two panels show some evidence of σ_o changes at SST fronts. Theoretically predicted values are presented in Table 7 and found to be in accordance with the observations. During the ERS-1 overpass the air-temperature was by 0.4°C higher than the water temperature at the position of NRV *Alliance* (Fig. 10), in accordance with the assumptions for Table 7. SST is found to exceed the channel-4 brightness temperature by 2.8°C, but this is of no importance for the prediction of σ_o.
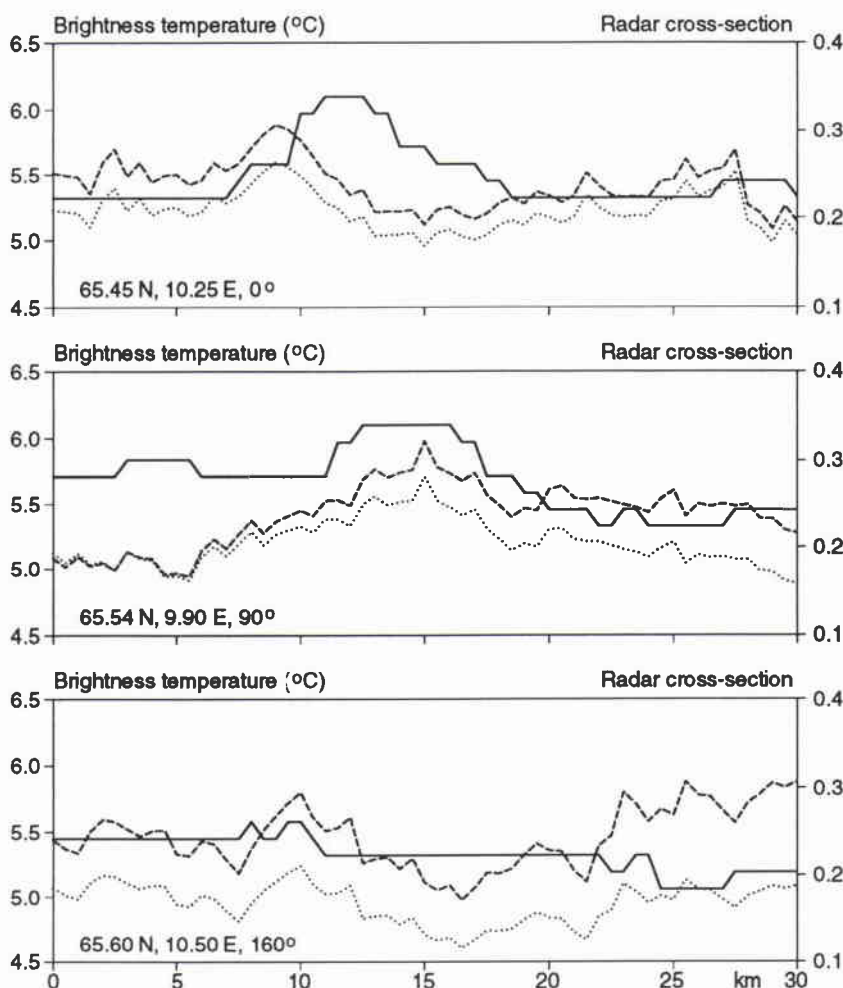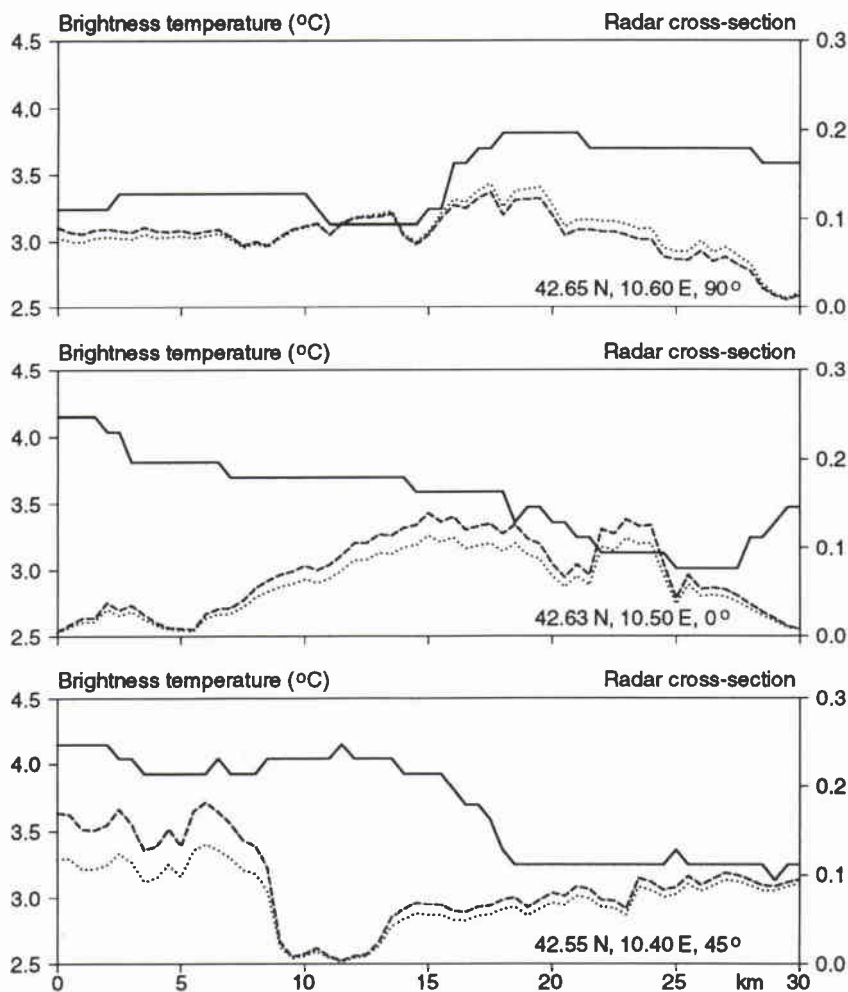
Figure 23: *Comparison of radar-cross sections (dashed lines) and brightness temperatures (full lines) along three 30 km sections in the Elba area, extracted from Figs. 9 and 11. Starting point and orientation are indicated. The σ_o values are means within 500×500 m resolution cells. Values corrected by Eq. (23) for $23°$ incidence angle (dotted lines).*

σ_o-model	U	$T_a - T_{w1}$	$T_a - T_{w2}$	σ_{o1}	$\Delta\sigma_o$
CMOD4	3.0 ms^{-1}	0.0°C	0.6°C	0.146	-0.015
IFREMER	3.0 ms^{-1}	0.0°C	0.6°C	0.163	-0.022
CMOD4	2.0 ms^{-1}	0.0°C	0.6°C	0.100	-0.023
IFREMER	2.0 ms^{-1}	0.0°C	0.6°C	0.093	-0.045

Table 7: *Theoretically predicted differences of the radar cross-section $\Delta\sigma_o = \sigma_{o2} - \sigma_{o1}$ across a temperature front $\Delta T = T_{w2} - T_{w1}$ for two different wind speeds. The computations refer to data from the Elba area, presented in Fig. 23.*

4.3   Surface currents

The spectrum of short waves, which cause radar backscatter, may be modulated by underlying currents. Theories, presented in Section 2.3, relate variations of the radar cross section to horizontal derivatives of surface current velocity. The prediction of σ_0 changes requires knowledge of the spatial variability of surface currents. Unfortunately, this is hard to measure and no *in situ* data are available for the SAR images under investigation. For the purpose of predicting σ_o changes, Annex D presents three current fields, which differ by the magnitude of horizontal derivatives, each by one order of magnitude.

The first current field (Fig. D1 in Annex D) is an eddy in Norwegian coastal waters, recorded in March 1985 by the land-based HF radar CODAR (Coastal radar) of the University of Hamburg [16]. The horizontal derivatives reach amplitudes of 10^{-4} s^{-1}. The measuring system performs averaging over some 3 × 3 km and may smooth out steeper current changes. The comparison with an AVHRR image showed that the eddy surrounded a warm water cell.

Surface currents associated with internal waves are estimated by boundary wave theory (Fig. D2). The wavelength has been chosen in accordance with those observed in the SAR image of Fig. 17. CTD sections, carried out from NRV *Alliance* within an extended area, revealed a sharp pycnocline at a depth of about 40 m and a density difference of 2.6 kgm^{-3}. These data have been used to model the internal waves and associated surface currents of Fig. D2. The magnitude of the horizontal divergence is of the order of 10^{-3} s^{-1}. Internal waves near the continental shelf are mostly of tidal origin and highly nonlinear [17]. This means that the horizontal derivatives may exceed those of our linear model. However, Apel [17] proposes a maximum strain rate of 2 × 10^{-3} s^{-1}, which is close to our value.

Figure D3 presents results from an analytical model of current fronts with gradients of the order of 10^{-2} s^{-1}. Two fields are shown, with vanishing curl and vanishing divergence, respectively, but the same component $\partial u_x / \partial x$. According to the theory of first-order modulation (Section 2.3) this component dominates the imaging process and thus, the SAR images of both fields should not be distinguishable.

Observed changes of radar cross section are displayed in Figs. 24-26. These will be compared with values estimated from the current fields presented. Figure 24 displays σ_o data along three sections in Norwegian coastal waters, extracted from the SAR image of Fig. 6b. The dotted lines refer to values corrected fc
incidence at $\vartheta_m = 23°$, Eq. (23). All sections pass through the position 65.55°N, 10.20°E, which is the centre of a warm water cell (Fig. 7b). It is assumed that this cell is surrounded by eddy-like currents [16].
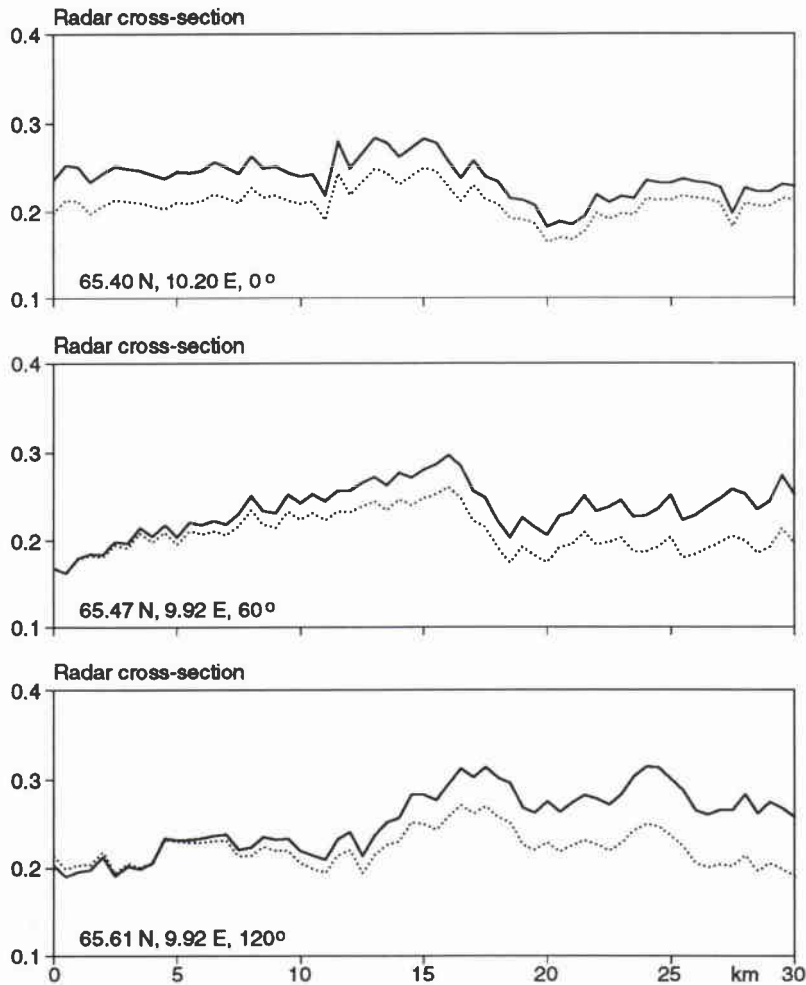
Figure 24: *Radar-cross sections along three 30 km sections in Norwegian coastal waters, extracted from Fig. 17. Starting point and orientation are indicated. At 15 km all sections pass through 65.54°N, 10.20°E. The σ_o values are means within 500 × 500 m resolution cells. Values corrected by Eq. (23) for 23° incidence angle (dotted lines).*

Figure 25 displays values of σ_o along sections through the wave-like structures of Fig. 17, a SAR image of the Strait of Messina. The position of NRV *Alliance* during the satellite overpass was some 200 km south-east of the centre of the imaged area (Fig. 14). Meteorological data are presented in Fig. 18 and will be used for subsequent analysis. The extremely strong variations of σ_o in the lower panel of Fig. 25 are most probably due to meteorological effects and will not be considered in the subsequent analysis of the imaging of internal waves.

Figure 25: *Radar-cross sections along three 20 km sections in the Strait of Messina, extracted from Fig. 17. Starting point and orientation are indicated. The σ_o values are means within 250×250 m resolution cells. Values corrected by Eq. (23) for $23°$ incidence angle (dotted lines).*

Figure 26 shows values of σ_o along west-east orientated sections through the light bands in the SAR image of Fig. 15, which are probably caused by current fronts. The position of NRV *Alliance* was some 400 km west of the imaged area (Fig. 14). Ship-measured meteorological data are presented in Fig. 16.
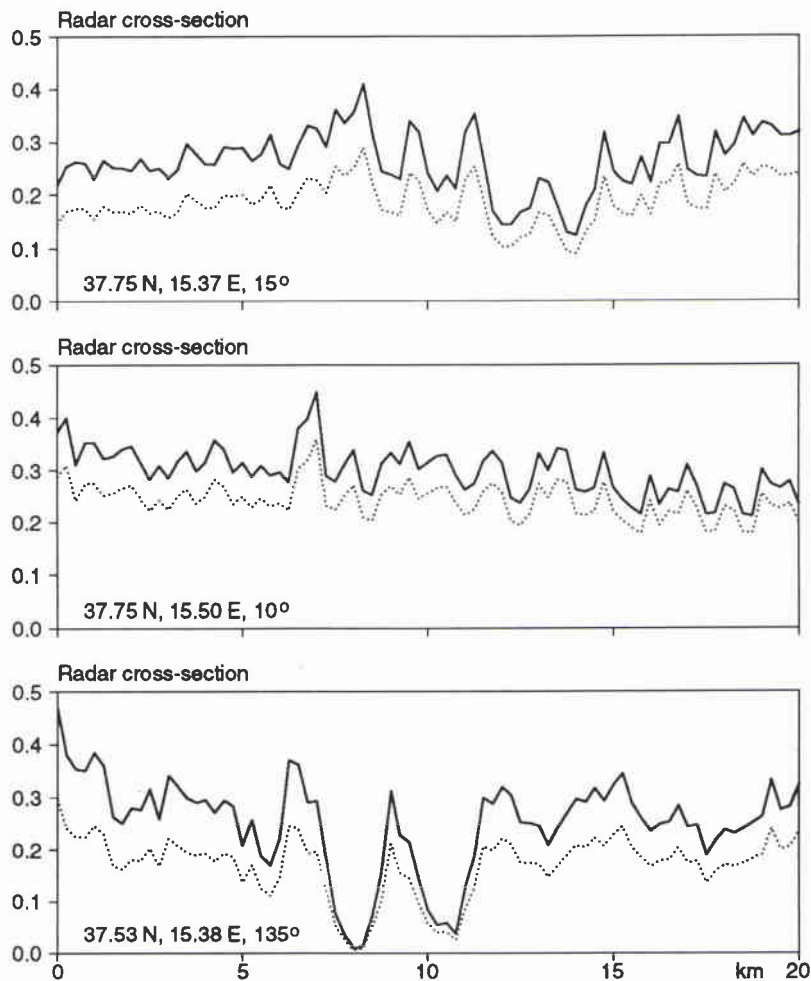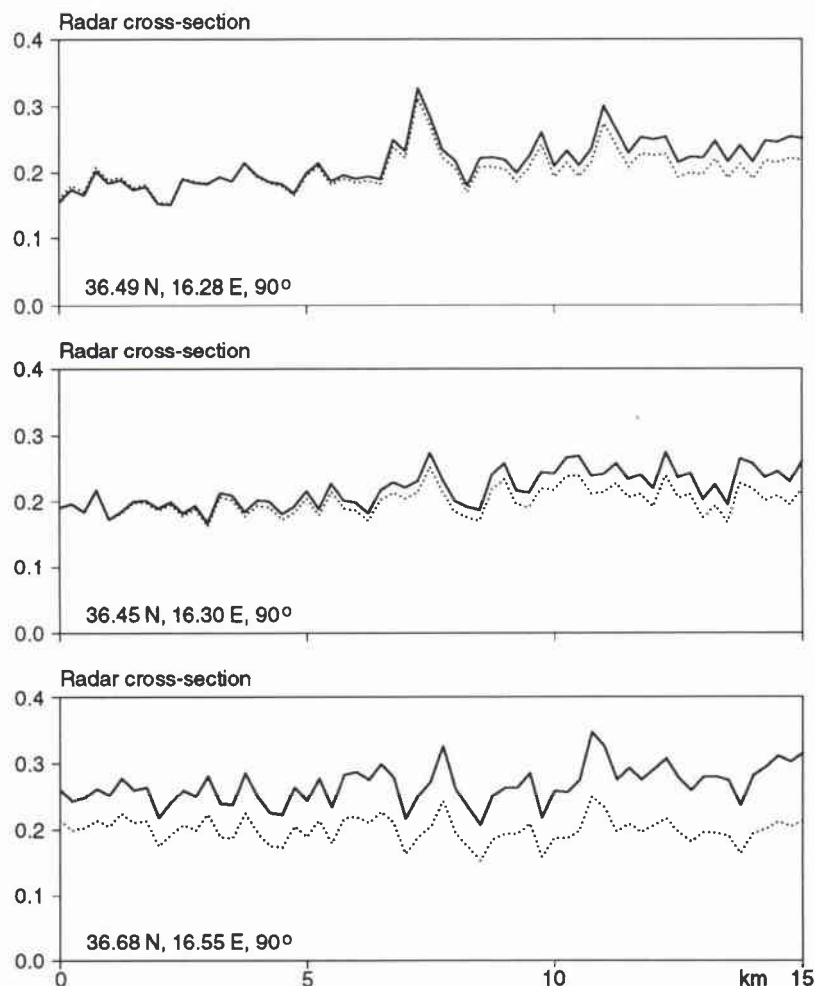
Figure 26: *Radar-cross sections along three 15 km sections south of the Strait of Messina, extracted from Fig. 15. Starting point and orientation are indicated. The σ_o values are means within 250×250 m resolution cells. Values corrected by Eq. (23) for $23°$ incidence angle (dotted lines).*

Before applying the theories of Section 2.3, the modulation of σ_o by changes of the wind velocity relative to the moving sea surface is investigated. Figure 2 demonstrates that σ_o-models are very sensitive to wind speed and direction. Assuming a homogeneous wind, the underlying currents cause variations in the relative wind and in turn the radar cross section. Figure 27 demonstrates the effect for the eddy of Fig. D1, i.e. the example with the strongest currents. The σ_o-model of IFREMER has been applied, CMOD4 yields similar results. By comparing the predicted σ_o changes with the measured values of Fig. 24 it is found that they are too small, by at least a factor of 2. It is remarkable that this simple mechanism (referred to as zero-order modulation) yields such significant results.
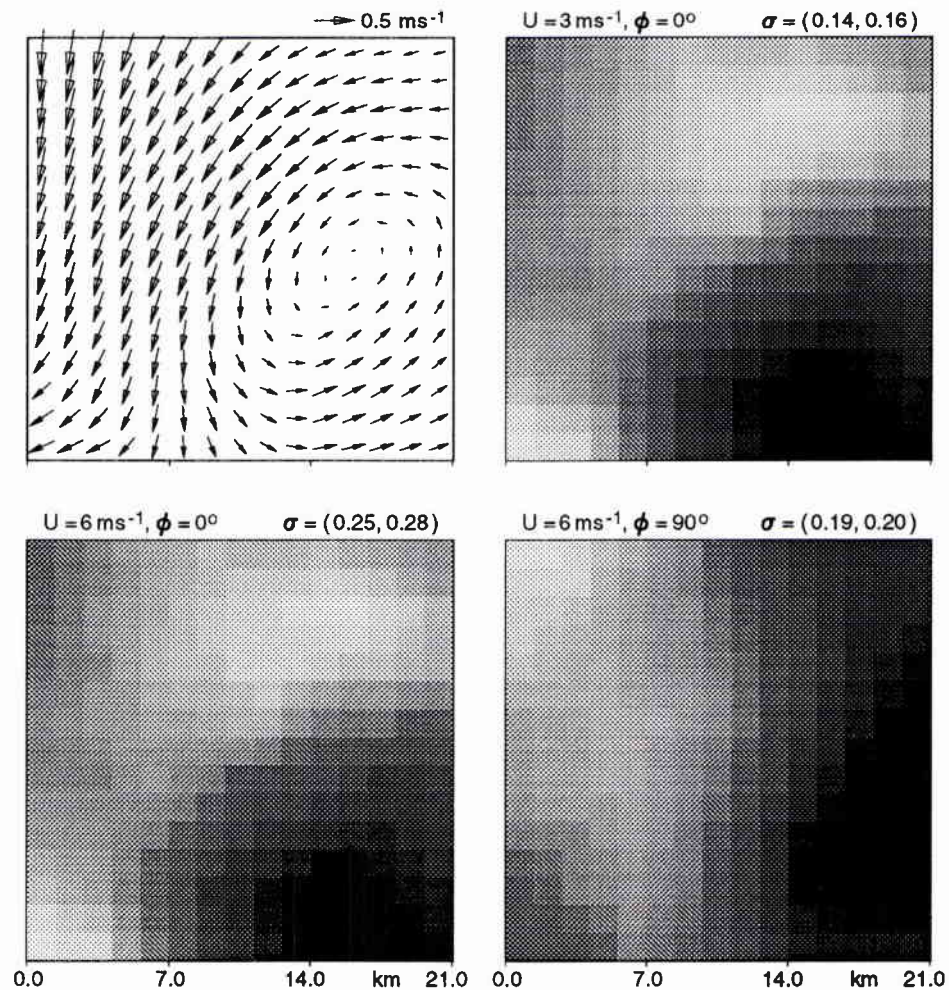
Figure 27: *Surface currents (eddy) and modulations of the radar-cross section for different wind speeds U and directions φ. The σ₀ values have been determined from the IFREMER model using the wind velocity relative to the current. Minimum and maximum values of σ₀ are indicated.*

First-order modulation

By making use of the current fields in Annex D, the spatial variability of σ_o is predicted with help of Eqs. (8)-(9). The coefficients in Eq. (9) are determined as described, solutions are obtained by Fourier methods. In many cases the advective terms on the left side of Eq. (9) can be disregarded and Eqs. (8)-(9) simplify to,

$$\frac{\sigma_1}{\sigma_o} = -\frac{1}{\mu}[(\gamma_v + \gamma_x)\frac{\partial u_x}{\partial x} + \gamma_y\frac{\partial u_x}{\partial y}], \tag{24}$$

which, as the comparison with the Fourier solutions shows, is an excellent approximation for the current fields considered.

As shown in Section 2.3, γ_y is small as compared to γ_x, which means that the changes of σ_o are proportional to those of $\partial u_x / \partial x$. From our examples, the current front of Fig. D3 reveals the highest values of this quantity. Figure 28 displays the current field together with the predicted radar cross section for three different winds. Though the current front is very acute (almost unrealistic), the corresponding changes in σ_o are relatively small and do not explain those observed in Fig. 15 and displayed along three sections in Fig. 26.
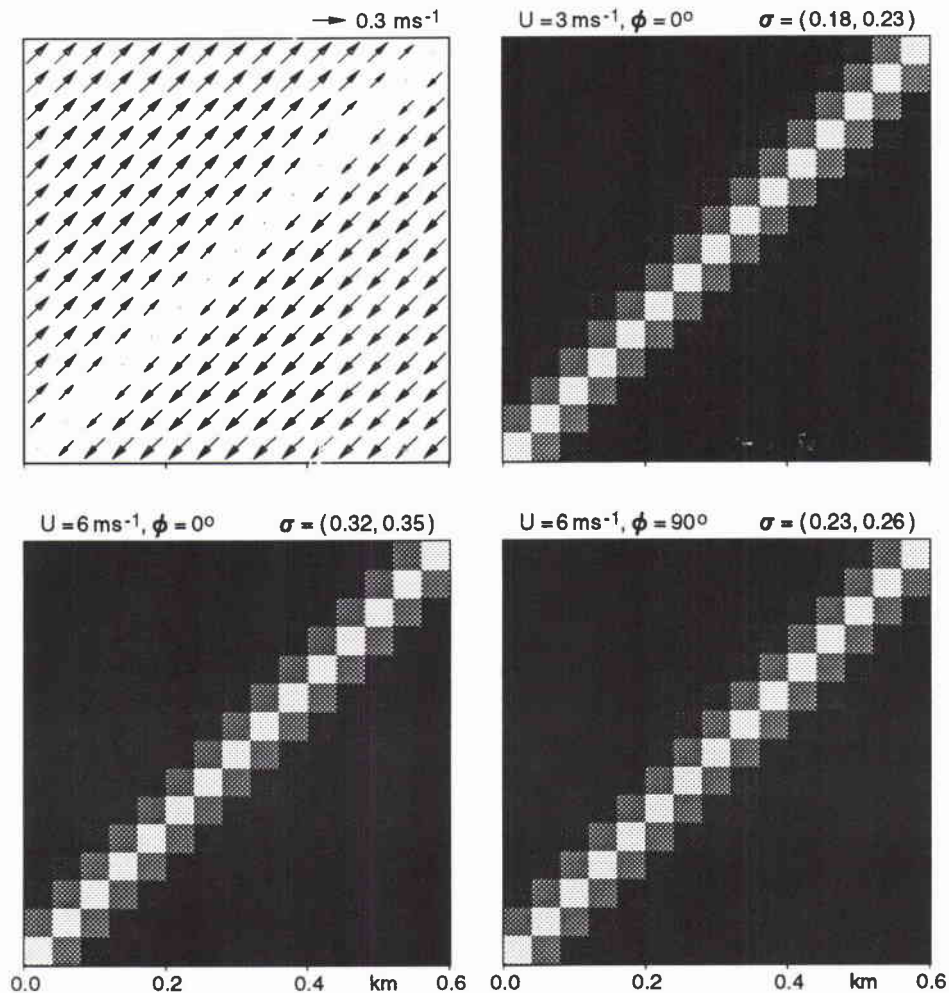

Figure 28: *Surface currents (front) and first-order modulations of the radar-cross section for different wind speeds U and directions ϕ. Minimum and maximum values of σ_o are given.*

Values of $\partial u_x/\partial x$ are by one or two orders of magnitude smaller for the internal wave field (Fig. D2) and the eddy field (Fig. D1), respectively, as are the predicted changes in σ_o. However, the observed changes in Fig. 24 and Fig. 25, which are assumed to be caused by eddies or internal waves, are of the same order as those for the front in Fig. 26. From these results it can be concluded that the theory of first-order modulation is not able to explain the observed σ_o changes in C-band SAR images caused by current features.

Second-order modulation

The determination of second-order modulations started with the two-dimensional Pierson-Moskowitz spectrum, Eq. (19), of the intermediate waves, which is determined by wind speed and direction. According to Eq. (20), surface currents modulate the spectrum. Considering the examples of current fields in Annex D, the modulated spectrum was calculated for each grid point by means of spatial Fourier transformation. In order to avoid discontinuities resulting from the Fourier decomposition, extended current fields were used with constant velocities at the edges (Annex D).

For numerical calculations the Pierson-Moskowitz spectrum, Eq. (19), was represented by a matrix of 15 wavenumbers by 11 directions. Wavenumbers are from the wavelength interval [0.5 m, 20 m], i.e. the wavelengths are shorter than the SAR resolution. In order to ensure numerical stability the wavenumber of the spectral peak was taken as the lower bound, in instances the corresponding wavelength was shorter than 20 m. Because of the steep fall-off, Eq. (19), only directions within $\pm 60°$ of the mean wind are considered. As Eq. (20) has been evaluated by means of a perturbation approach (Annex C), the solutions E_1 should be smaller than E_o. This is not the case for the current fronts of Fig. D3. Thus, the application of the theory was confined to the current fields of Fig. D1 (eddy) and Fig. D2 (internal wave field).

Having determined the modulated wave-number spectrum, the integration by means of Eq. (18) yields the modulated radar-cross section for each current grid point. The importance of the three different terms, referring to orbital motion and both slope components of the intermediate waves, is shown in Table 5. The dominant contributions are from the slope components parallel to the radar look direction, which is the x-axis (Fig. 1). The distribution of the slope components is determined by the wind direction *via* the Pierson-Moskowitz spectrum, Eq. (19). Hence, the wind direction strongly influences σ_o modulation.

Figure 29 displays the results for the Fig. D1 eddy in Annex D. Three wind directions are considered for a fixed wind speed of 6 ms^{-1}. Only for the wind blowing parallel to the radar look direction is there measurable σ_o variability, but less than that observed (Fig. 24). Comparing this case with the of zero-order modulation in Fig. 27, it is

found that not only σ_o has increased but also that both images are different. As SAR views the changes of only one component of the two-dimensional current field, the images give no indication of the presence of an eddy. The theory of second-order modulation predicts increasing relative σ_o variability with increasing wind speed, but also higher σ_o values than the measured ones of Fig. 24.

Figure 29: *Surface currents (eddy) and second-order modulations of the radar-cross section for a fixed wind speed U and different wind directions ϕ. Minimum and maximum values of σ_o are given.*

Figure 30 shows good agreement between predicted and measured σ_o variability (Fig. 25, upper panel) due to internal waves. A fixed wind speed of 6 ms^{-1} and three different wind directions have been considered. For the wind perpendicular to the radar look direction ($\phi = 90°$), changes in σ_o are minimal which confirms the necessity of knowing the wind direction when extracting quantitative information from SAR images. Although the modelled SAR images give the impression of reproducing

the two-dimensional current field, they mainly reflect changes in $\partial u_x/\partial x$.

It may therefore be stated that by taking into account the intermediate wave field (second-order modulation) the agreement between predicted and measured C-band σ_o variability caused by currents is improved.
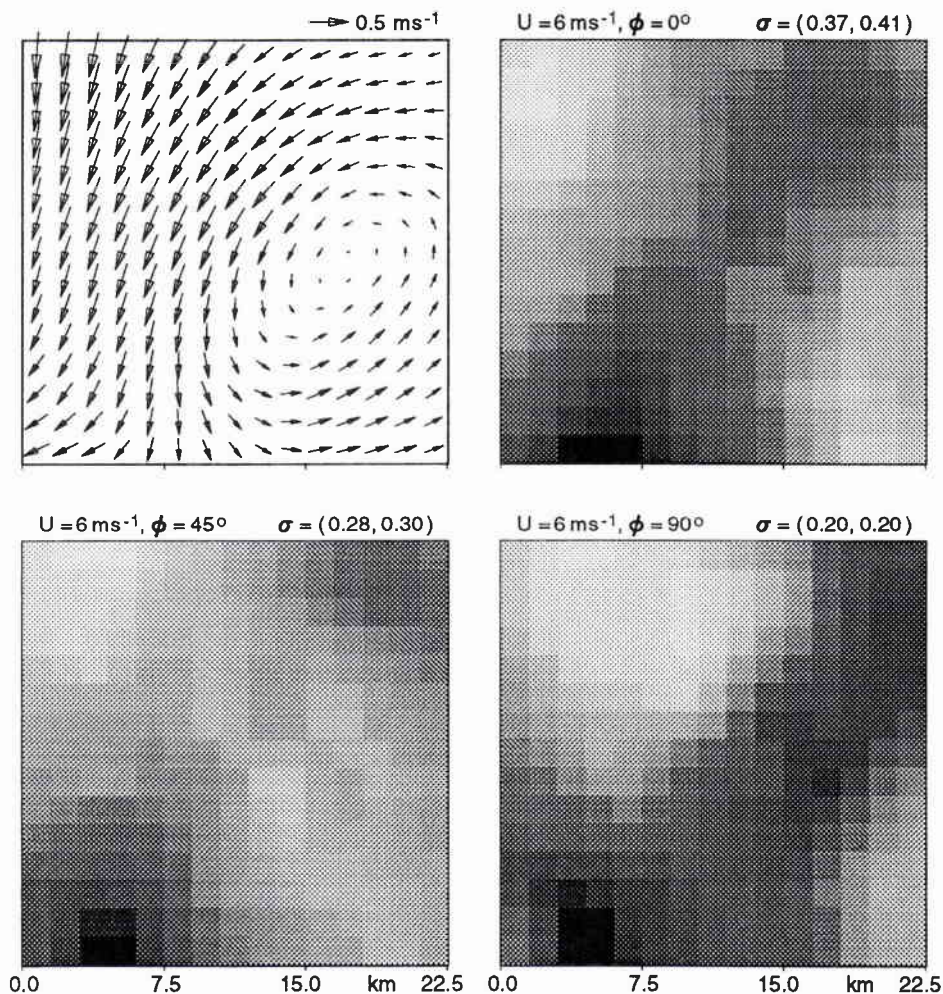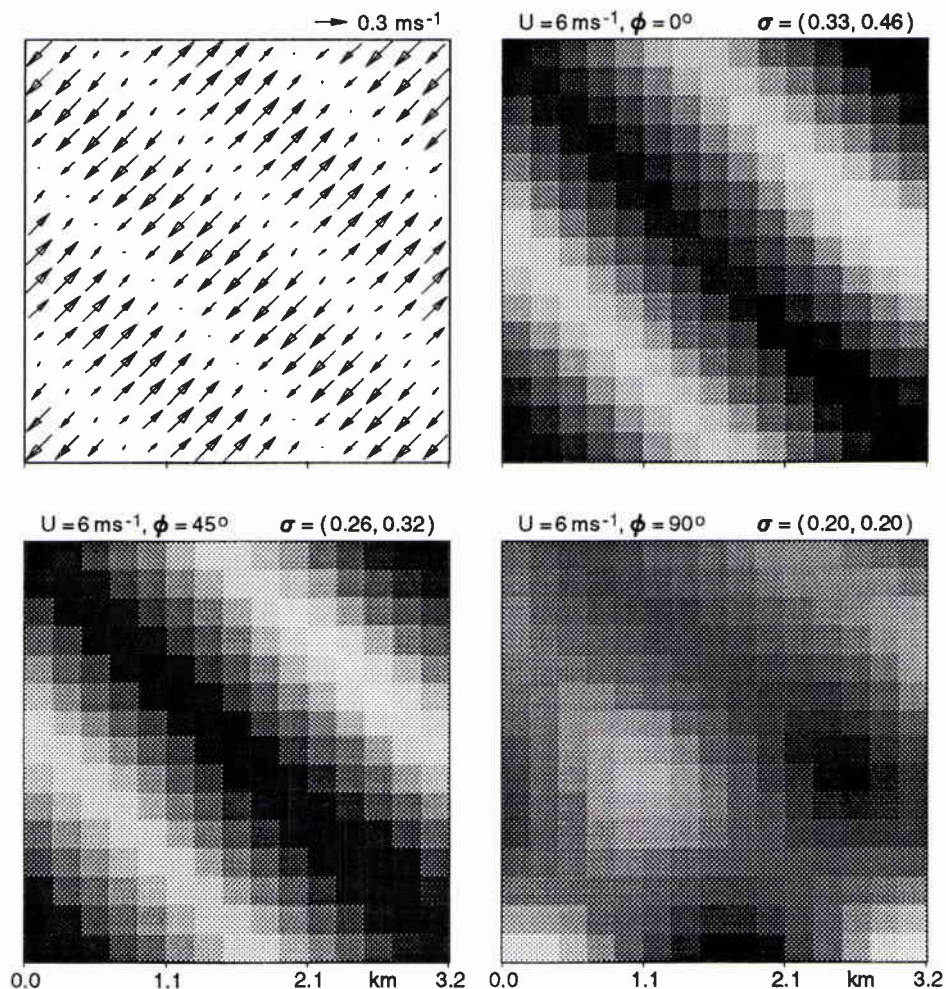

Figure 30: *Surface currents (internal waves) and second-order modulations of the radar-cross section for a fixed wind speed U and different wind directions ϕ. Minimum and maximum values of σ_o are given.*

5

Conclusions

Synthetic aperture radar (SAR) images of the first European remote sensing satellite (ERS-1) were acquired and analysed. C-band SAR takes high-resolution (about 30 m) images of the sea-surface. Unlike sensors operating in the visible or infrared band, microwave SAR is not affected by cloud cover. Notwithstanding backscatter due to small-scale sea surface roughness, SAR is highly suited to the imaging of mesoscale oceanic features. The investigations emphasized the extent to which quantitative information can be obtained from SAR imagery.

Empirical dependencies (σ_o-models) of the radar cross section on the surface-wind vector were determined for the ERS-1 scatterometer, which operates at the same frequency as the SAR. By making use of these models, wind speeds have been calculated from SAR images of Norwegian coastal waters and the area south of Elba in the Mediterranean. A reliable estimate requires *a priori* knowledge of wind direction, which was available either from analyzed wind fields (Norwegian coast) or ship measurements (Elba). Good agreement between satellite-retrieved and *in situ* wind speeds was found, with the exception of the case when a thunderstorm passed by. The retrieved value considerably underestimates the real wind, obviously due to rainfall. The same may occur in case of snowfall, as Essen [18] found by comparing winds retrieved from the scatterometer of ERS-1 and ship measurements. Apart from these unusual weather situations, SAR imagery can help to study spatial wind variability on smaller scales than with the scatterometer, which allows a resolution of only 50 km.

The comparison of SAR images with sea-surface temperature (measured by the satellite-borne AVHRR), revealed remarkable relationships [1]. For this reason, the capability of imaging thermal fronts has been investigated by applying theories of boundary-layer stability and SAR imagery. Changes in SST cause changes in the surface wind stress, which (instead of the wind speed) is assumed to strongly influence the radar cross section. The estimation of σ_o changes requires homogeneity of both the wind field and air temperature across the SST front, which is unrealistic. In some cases numerical results were found to be in approximate agreement with observations. On the other hand, changes of σ_o of the same order exist without any SST variability, caused by other physical processes. Hence, the separation of the various influences on σ_o is the main difficulty in extracting quantitative information from SAR images.

Emphasis has been placed on the possibility of determining changes in surface current from SAR images. As no *in situ* data are available for the SAR images under investigation, three model current fields are used for numerical investigations, which differ by the magnitude of horizontal derivatives, each by one order of magnitude. Considering a homogeneous wind, surface currents modify the relative wind and in turn the radar-cross section dependence on the (relative) wind vector. For the strong current associated with an eddy, this zero-order modulation leads to visible changes in σ_0, which however are too small at least by a factor of 2. The zero-order modulation does not explain the visibility of internal waves and current fronts in SAR images.

The scattering small-scale surface (Bragg) waves are modulated by underlying currents. Theories based on this first-order modulation, successfully explained the imaging of bottom topography in areas of strong tidal currents [7] and of internal waves with L-band SARs [8,17]. It has been found that this theory is not able to reproduce the observed σ_o changes in the C-band SAR images investigated [9]. Better results could be achieved with the theory of second-order modulation, which takes into account the influence of the intermediate wave spectrum, i.e. waves which are longer than the scattering Bragg waves but smaller than the resolution of the SAR. However, this theory requires knowledge of the wind direction and the two-dimensional spectrum of intermediate waves.

The possibility of extracting quantitative information from SAR images is limited for two reasons. First, the theories require the knowledge of parameters, which are either not available or not available to sufficient degree of accuracy (as the intermediate wave spectrum for the theory of second-order modulation). Secondly, the observed features are a result of more than one process (current fronts probably coincide with thermal fronts). However, with supplementary information from other satellite sensors and/or *in situ* measurements, SAR images can be helpful towards an improved understanding of mesocale processes in the ocean.

References

[1] Johannessen, J.A., Shuchman, R.A., Johannessen, O.M. (1995). Synthetic aperture radar on ERS-1. *In:* Ikeda, M., Dobson, F.W. (eds.) Oceanographic applications of remote sensing. Boca Raton, FL., CRC Press.

[2] Johannessen, J.A., Shuchman, R.A., Wackerman, C., Digranes, G., Lyzenga, D., Johannessen, O.M. (1993). Detection of surface current features with ERS-1 SAR. *In:* Proceedings 2nd ERS-1 Symposium, Hamburg, Germany ,11-14 October, 1993.

[3] Valenzuela, G.P. (1978). Theories for the interaction of electromagnetic and ocean waves - a review. *Boundary-Layer Meteorology*, **13**, 61-85.

[4] Ulbay, F.T., Moore, R.K., Fung,A.K. (1986). Microwave remote sensing III: from theory to application. Washington, D.C., Artech House Inc.

[5] Phillips, O.M. (1977). The dynamics of the upper ocean (second edition). Cambridge, Cambridge University Press.

[6] Askari, F., Geernaeft, G.L., Keller, W.C., Raman. R. (1993). Radar imaging of thermal fronts. *International Journal of Remote Sensing*, **14**, 275-294.

[7] Alpers, W., Hennings, I. (1984). A theory of the imaging mechanism of underwater bottom topography by real and synthetic aperture radar. *Journal of Geophysical Research*, **89**, 10529-10546.

[8] Alpers, W. (1985). Theory of radar imaging of internal waves. *Nature*, **314**, 245-247.

[9] Lyzenga, D.R. (1991). Interaction of short surface and electromagnetic waves with ocean fronts. *Journal of Geophysical Research*, **96**, 10765-10772.

[10] Hasselmann, K. (1971). On the mass and momentum transfer between short gravity waves and larger scale motion. *Journal of Fluid Mechanics*, **50**, 189-205.

[11] Romeiser, R. (1993). Eine verbesserte Theorie zur Modulation der Radar-Rückstreuung von der Meeresoberfläche auf der Basis eines Drei-Skalen-Modells. PHD thesis, Universität Bremen, Germany. [An improved modulation theory for radar backscattering from the sea surface based on a three dimensional model].

[12] Romeiser, R., Alpers, W. (1994). An improved two-dimensional composite surface model for the radar imaging of uderwater bottom topography. Submitted to *Journal of Geophysical Research*.

[13] Pierson, W.J., Moskowitz, L. (1964). A proposed spectral form for fully developed wind seas based on the similarity theory of S.A. Kitaigorodskii. *Journal of Geophysical Research*, **69**, 5181-5190.

[14] Laur, H. (1992). Derivation of backscattering coefficient σ_o in ERS-1.SAR.PRI products. European Space Agency (ESA) reference document.

[15] Minnett, P.J. (1991). Surface measurements made during the Icelandic Current Experiment (ICE 89) from the R/V *Alliance*, SACLANTCEN SM-247. La Spezia, Italy, SACLANT Undersea Research Centre.

[16] Essen, H.-H. (1995) Geostrophic surface currents as derived from satellite SST images and measured by a land-based HF radar. *International Journal of Remote Sensing*, **16**, 239-256.

[17] Apel, J.R. (1995). Linear and nonlinear internal waves in coastal and marginal seas. *In:* Ikeda, M., Dobson, F.W. (eds.) Oceaonographic applications of remote sensing. Boca Raton, FL., CRC Press.

[18] Essen, H.-H. (1994). Sea-surface winds in the Iceland-Faeroe area, as derived from the ERS-1 scatterometer, SACLANTCEN SR-220. La Spezia, Italy, SACLANT Undersea Research Centre.

[19] Quilfen, Y. (1992). Validation and quality of ERS-1 scatterometer wind data. *In:* Proceedings, ERS-1 Geophysical Validation Workshop, Penhors, Bretagne, France.

[20] Lecomte, P. (1993). CMOD-4 model description. European Space Agency, Doc.No.: ER-TN-ESA-GP-1120.

[21] Smith, S.D. (1988). Coefficients for sea surface wind stress, heat flux and wind profiles as a function of wind speed and temperature. *Journal of Geophysical Research*, **93**, 15467-15472.

[22] LeBlond, P.H., Mysak, L.A. (1978) Waves in the ocean. Amsterdam, Elsevier.

[23] Alpers, W., Hasselmann, K. (1978) The two-dimensional microwave technique for measuring ocean-wave spectra from an airplane or satellite. *Boundary Layer Meteorology* **13**, 215-230.

[24] Hughes, B.A. (1978). The effect of internal waves on surface wind waves. 2. Theoretical analysis. *Journal of Geophysical Research*, **83**, 455-465.

A

C-band scatterometer models

Two models of the linear radar cross section σ_o are presented, which both have been developed for the C-band scatterometer. The modelled σ_0 depends on the incidence angle ϑ [deg] of the radar antenna and the wind speed U [ms^{-1}] and wind direction ϕ [deg], which is defined relative to the direction of the SAR beam, i.e. is zero when the wind blows towards the satellite (Fig. 1, main text).

1) IFREMER: This model has been tuned with σ_o measurements of the ERS-1 scatterometer and wind data from NOAA buoys around the coasts of the USA (Quilfen [19]):

$$\sigma_o = b_o[1 + b_1 \cos\phi + b_2 \cos(2\phi))],\qquad(A1)$$

with,

$$b_o = 10^{\alpha+\beta\sqrt{U-\delta}},$$

$$\alpha = c_1 + c_2 P_1 + c_3 P_2 + c_4 P_3, \quad \beta = c_5 + c_6 P_1 + c_7 P_2, \quad \delta = c_8 + c_9 P_1 + c_{10} P_2,$$

$$b_1 = c_{11} + c_{12} P_1 + c_{13} U,$$

$$b_2 = c_{14} + c_{15} P_1 + c_{16} P_2 + (c_{17} + c_{18} P_1 + c_{19} P_2)U + c_{20} U^2,$$

where,

$$P_1 = (\vartheta - 36)/19, \quad P_2 = (3P_1^2 - 1)/2, \quad P_3 = (5P_1^2 - 3)P_1/2.$$

2) CMOD4: This model is presently used by ESA to retrieve surface winds from the ERS-1 scatterometer (Lecomte [20]). It has been tuned using global meteorological model data provided by the European Centre for Medium-Range Weather Forecast (ECMWF):

$$\sigma_o = b_o[1 + b_1 \cos\phi + b_3 \tanh(b_2)\cos(2\phi)]^{1.6},\qquad(A2)$$

with,

$$b_o = \delta \times \begin{cases} 10^{\alpha} & \text{if, } U + \beta \leq 0, \\ 10^{\alpha}(U + \beta)^{\gamma} & \text{if, } 0 < U + \beta \leq 5, \\ 10^{\alpha+0.3125\gamma\sqrt{U+\beta}} & \text{if, } 5 < U + \beta, \end{cases}$$

$$\alpha = c_1 + c_2 P_1 + c_3 P_2, \quad \beta = c_4 + c_5 P_1 + c_6 P_2, \quad \gamma = c_7 + c_8 P_1 + c_9 P_2,$$

$$b_1 = c_{10} + c_{11} U + [\tanh(2.5(P_1 + 0.35)) - 0.61(P_1 + 0.35)](c_{12} + c_{13} U),$$

$$b_2 = c_{14} + c_{15}(1 + P_1)U,$$

$$b_3 = 0.42(1.0 + c_{16}(3 + P_1)(U - 10)),$$

where,

$$P_1 = (\vartheta - 40)/25, \quad P_2 = (3P_1^2 - 1)/2.$$

and δ is a bias correction given as function of ϑ with 1° resolution.

B

Atmospheric boundary layer

According to Smith [21] the wind profile $U(z)$ within the atmospheric boundary layer can be described by,

$$U(z) = \frac{u_*}{\kappa}[\ln \frac{z}{z_o} - \psi(\frac{z}{L})], \qquad (B1)$$

where $\kappa = 0.4$ is the Karman constant. The Monin-Obukhov length L and the roughness height z_0 are given by,

$$L = \frac{T_w u_* U}{\kappa g (T_a - T_w)}, \quad z_o = 0.011 \frac{u_*^2}{g}, \qquad (B2)$$

where g $= 9.8$ ms^{-2} is the gravity acceleration, T_w and T_a (measured in K) are the temperature of water and air, respectively. The stability function ψ is,

$$\psi = -5.0\frac{z}{L} \quad if, \quad \frac{z}{L} > 0 \; (stable),$$

$$\psi = 2\ln\frac{1+x}{2} + \ln\frac{1+x^2}{2} - 2tan^{-1}x + \frac{\pi}{2} \quad if, \quad \frac{z}{L} < 0 \; (unstable),$$

$$with, \quad x = (1 - 16\frac{z}{L})^{\frac{1}{4}}. \qquad (B3)$$

These equations implicitly determine u_* for a given wind speed at height z and the temperature difference $T_a - T_w$, which is assumed to be independent of height. Numerical values are obtained by means of a simple search algorithm.

C

Hydrodynamic modulation

As discussed in Section 2, radar imagery of the sea surface at incidence angles between $20°$ and $60°$ is due to Bragg scattering, i.e. the images reflect the distribution of short surface waves of some 10 cm wavelength. Underlying currents may modulate these short waves and in turn influence the radar cross section. Most likely, this is the mechanism by which surface motions become visible in SAR images. Currents to be considered are the orbital motion of long ocean waves (swell) as well as surface currents associated with internal waves, tides, fronts, eddies, etc.

For theoretical purposes, the underlying currents can be treated as a slowly varying mean field, which is nearly constant over distances of the order of the short scattering wavelengths. The change of the short-wave spectrum is determined by the action balance equation, cf. LeBlond and Mysak [22],

$$\left(\frac{\partial}{\partial t} + \dot{x}_\alpha \frac{\partial}{\partial x_\alpha} + \dot{k}_\alpha \frac{\partial}{\partial k_\alpha}\right) N(\mathbf{k}, \mathbf{x}, t) = S(\mathbf{k}, \mathbf{x}, t), \qquad (C1)$$

where $N(\mathbf{k}, \mathbf{x}, t) = F(\mathbf{k}, \mathbf{x}, t)/\omega_o$ is the action spectrum and, ω_o the intrinsic frequency of the short waves, and $F(\mathbf{k})$ the two-dimensional wave-height spectrum as used in Eq. (3). Bold letters represent horizontal two-dimensional vectors, the components of which are marked by indices α or β. Summation has to be performed over double indices. The apparent frequency ω for an observer in rest is,

$$\omega(\mathbf{k}, \mathbf{x}, t) = \omega_o(\mathbf{k}) + k_\alpha u_\alpha(\mathbf{x}, t), \qquad (C2)$$

where $\mathbf{u}(\mathbf{x}, t)$ denotes the current velocity at the sea surface, and ω_o depends on $|\mathbf{k}|$ by the disperison relation, Eq. (2). The waves propagate along trajectories given by,

$$\dot{x}_\alpha = \frac{\partial \omega}{\partial k_\alpha} = v_{g\alpha} + u_\alpha, \quad \dot{k} = -\frac{\partial \omega}{\partial x_\alpha} = -k_\beta \frac{\partial u_\beta}{\partial x_\alpha}, \qquad (C3)$$

with $v_{g\alpha} = d\omega_o/dk_\alpha$ being the group velocity.

Assuming that currents introduce only small perturbations to the radiation balance, solutions of Eq. (C1) can be found by means of a perturbation expansion,

$$N(\mathbf{k}, \mathbf{x}, t) = N_o(\mathbf{k}) + N_1(\mathbf{k}, \mathbf{x}, t) + \dots \qquad (C4)$$

Following Alpers and Hasselmann [23], it is assumed that the source term is of order 1 and can be represented by,

$$S(\mathbf{k}, \mathbf{x}, t) = -\mu N_1(\mathbf{k}, \mathbf{x}, t), \qquad (C5)$$

where μ has the dimension of s^{-1} and can be interpreted as relaxation rate.

It may be assumed that N_1 varies with the time- and space-scales of the modulating field. Then, in the case of modulation due to long ocean waves, the local time deriviation dominates the left side of Eq. (C1), while the other terms can be treated as 1st order perturbations. Inserting Eqs. (C3)-(C5) into Eq. (C1), the 1st order equation becomes,

$$\left(\frac{\partial}{\partial t} + \mu\right) N_1 = k_\beta \frac{\partial u_\beta}{\partial x_\alpha} \frac{\partial N_o}{\partial k_\alpha}. \qquad (C6)$$

Considering surface currents, e.g. internal waves, the temporal variability is much slower (periods of hours instead of seconds) and the local time derivation becomes small as compared to the advective terms in the left side of Eq. (C1). Assuming that the spatial current changes are of 1.-order, we obtain,

$$\left((v_{g\alpha} + u_{o\alpha})\frac{\partial}{\partial x_\alpha} + \mu\right) N_1 = k_\beta \frac{\partial u_\beta}{\partial x_\alpha} \frac{\partial N_o}{\partial k_\alpha}, \qquad (C7)$$

where $\mathbf{u}_o$ is the mean current.

The relaxation rate μ is not a well known quantity. Estimates may differ by an order of magnitude. Following Romeiser [11], we use a simplified version of the parameterisation of Hughes [24],

$$\mu = \omega \frac{u_*}{v_p} \left(0.01 + 0.016 \frac{u_*}{v_p}\right) \left(1 - \exp(-8.9\sqrt{u_*/v_p})\right). \qquad (C8)$$

The dependence of the friction velocity μ_* on wind speed at a certain height, e.g. the reference height of $10m$, is given by the equations in Annex B. For moderate wind speeds and neutral stratification there exists a nearly linear dependence,

$$u_* = 0.03 \times U(10m). \qquad (C9)$$

D

Model current fields

The prediction of current-induced σ_o changes requires the knowledge of the horizontal variability of surface currents. Spatial current fields are difficult to measure and in general not available for the comparison with SAR images. Two-dimensional current fields can be measured by means of shore-based HF radars with a resolution of some 2 km. We will make use of such data in the context with eddies in Norwegian coastal waters. Surface currents associated with internal waves are estimated from the theory of boundary waves. Fronts are described by a simple analytic model.

Eddies

The inner frame of Fig. D1 displays surface currents as measured by CODAR (Coastal radar) in March 1985 at 59°N off the coast of Norway [16]. In order to avoid discontinuities at the edges, when applying Fourier techniques, the field has been extrapolated to a constant (mean) vector at the edges of the outer square. Shown are also the divergence and curl, as derived from central differences of the current field.

Internal waves

The measurements from onboard NRV *Alliance* in the Sicily area revealed a sharp pycnocline. With regard to this finding it is reasonable to describe the internal wave field by boundary waves at the interface of two layers with constant density each. Solutions of the linearised equations of motion and continuity are,

$$\zeta = \varphi(z)\exp\{i(\mathbf{kx} - \omega t)\} \quad with, \quad \varphi''(z) = \gamma^2\varphi(z), \quad \gamma^2 = \frac{\omega^2 k^2}{\omega^2 - f^2},$$

$$\mathbf{u} = [\omega k_x + ifk_y, \omega k_y - ifk_x]\frac{\varphi'(z)}{k^2}\exp\{i(\mathbf{kx} - \omega t)\},$$

$$u_z = -i\omega\varphi(z)\exp\{i(\mathbf{kx} - \omega t)\},$$

$$p = \rho(\omega^2 - f^2)\frac{\varphi'(z)}{k^2}\exp\{i(\mathbf{kx} - \omega t)\}. \tag{D1}$$
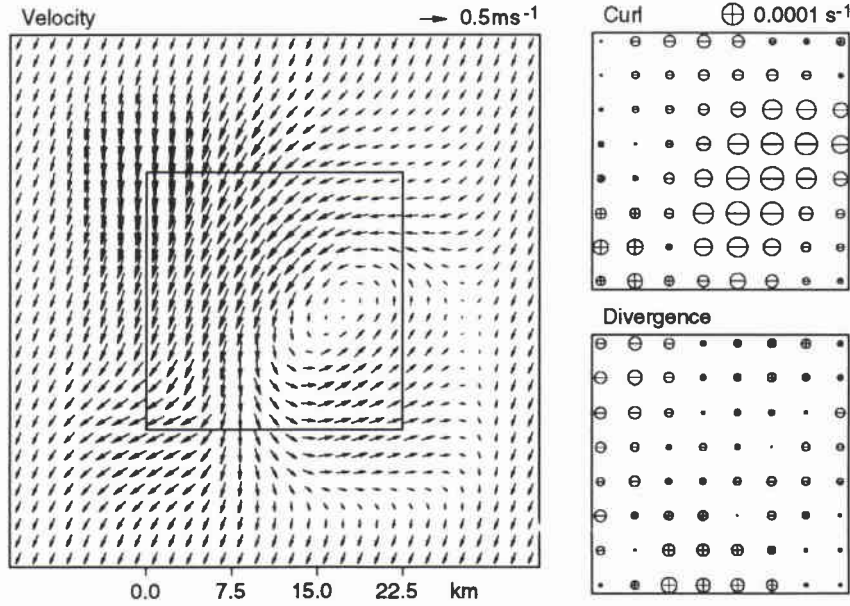
Figure D1: *Surface currents as measured by the land-based CODAR (Coastal radar) off the coast of Norway (59°N). The inner frame displays the measured velocities, which have been extrapolated to a constant (mean) vector at the edges of the outer frame. Curl and divergence of the inner frame are displayed in the right panels.*

where ζ is the vertical particle displacement, $[\mathbf{u}, u_z]$ the three-dimensional vector of particle velocity and p the departure from hydrostatic pressure. The Coriolis parameter f at the latitude Sicily is,

$$f = 8.8 \times 10^{-5} s^{-1}. \tag{D2}$$

We consider a two-layer model of the ocean, with the upper layer of density ρ_1 extending from $z = 0$ (sea surface) to $z = -d$ (depth of the pycnocline), and the lower of density ρ_2 from $z = -d$ to $z = -h$ (sea floor). We assume that there are no vertical motions at the sea surface and the sea floor,

$$\zeta_1(0) = \zeta_2(-h) = 0, \tag{D3}$$

where the indices refer to the two layers. At their boundary the kinematic and dynamic boundary conditions have to be fulfilled,

$$\zeta_2(-d) = \zeta_1(-d),$$

$$p_2(-d) = p_1(-d) + g(\rho_2 - \rho_1)\zeta(-d). \tag{D4}$$

From the first equation we obtain the dependence of the amplitude on depth,

$$\varphi(z) = \begin{cases} A sinh^{-1}(-\gamma d) sinh(\gamma z) & if, \ 0 \geq z \geq -d, \\ A sinh^{-1}(\gamma(h-d)) sinh(\gamma(h+z)) & if, \ -d \geq z \geq -h, \end{cases} \tag{D5}$$

where A is the amplitude of the internal wave at the pycnocline. The dispersion relation becomes,

$$\omega^2 = \frac{gk^2(\rho_2 - \rho_1)}{\gamma[\rho_2 coth(\gamma(h-d)) + \rho_1 coth(\gamma d)]} + f^2. \qquad (D6)$$

The current field of Fig. D2 refers to density jump of 2.6 kgm^{-3} at the depth of 40 m and an internal-wave amplitude of 15 m. Damping has been introduced in the outer frame in order to obtain zero currents at the edges. As estimated from the SAR image of Fig. 17 (main text), a wavelength of 2 km has been chosen. Surface currents are found to be nearly parallel to the wave vector, which points to 45°, i.e. the Coriolis force is of little influence.
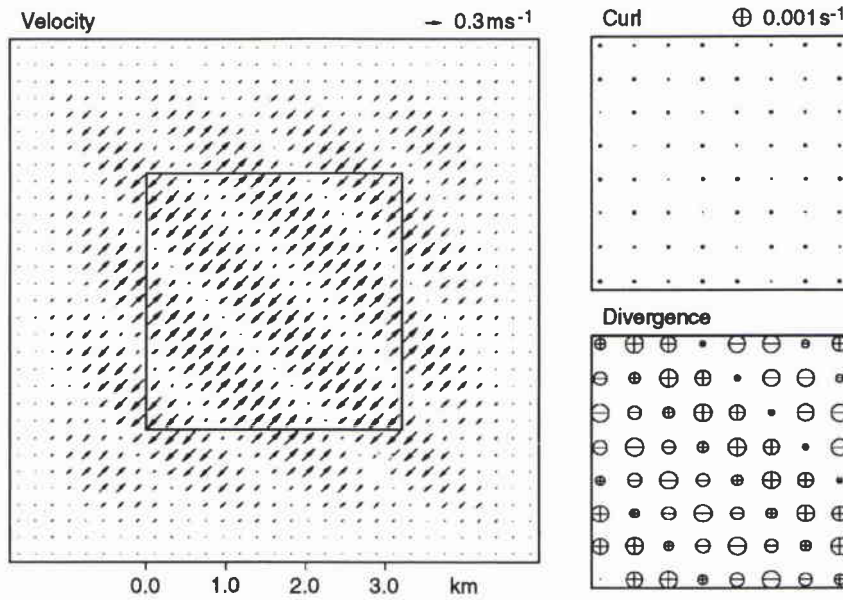

Figure D2: *Modelled surface currents induced by internal waves. The inner frame displays the linear field in accordance with Eqs. (D1-D6), which is damped to zero at the edges of the outer frame. Curl and divergence of the inner frame are displayed in the right panels.*

Fronts

SAR images often show light or dark stripes which most probably are due to current fronts. We use a simple analytic model to describe sharp but continuous changes in current velocity,

$$\mathbf{u} = \mathbf{u}_o + A tanh(a_o + \mathbf{a}x). \qquad (D7)$$

The location and extension of the front is determined by the argument of the *tanh*-function, the change in speed by the amplitude **A**. Figure D3 shows two examples,

one with vanishing divergence (upper panel) and the other with vanishing curl (lower panel). For both fields $\partial u_x/\partial x$ is the same.
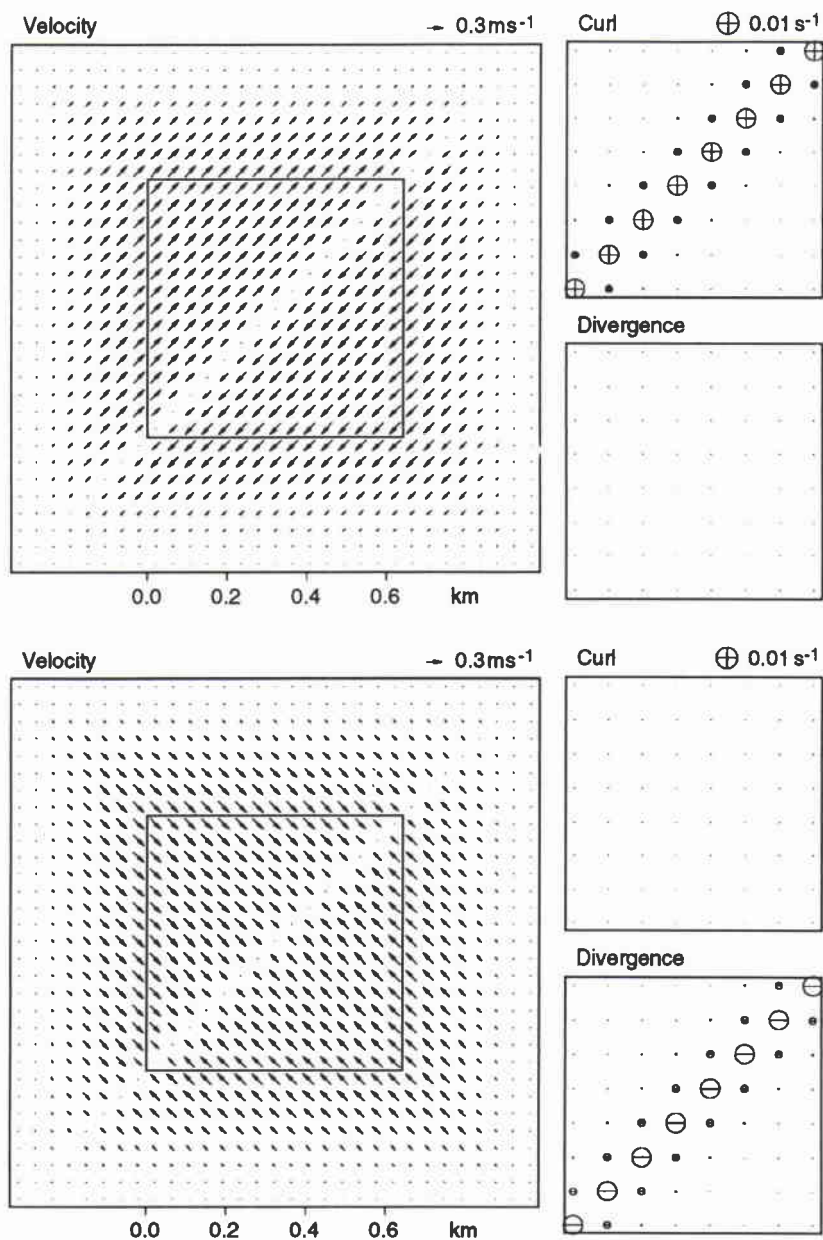

Figure D3: *Modelled fronts of surface current, with vanishing divergence (upper part) and vanishing curl (lower part). The inner frame displays velocities in accordance with Eq. (D7), which are damped to zero at the edges of the outer frame. Curl and divergence of the inner frame are displayed in the right panels.*

Document Data Sheet

Security Classification		Project No.
		23

Document Serial No.	Date of Issue	Total Pages
SR-247	February 1996	60 pp.

Author(s)

H.-H. Essen

Title

On the applicability of satellite-borne SAR imagery to coastal oceanography

Abstract

Synthetic aperture radar (SAR) images have been acquired from the first European Space Agency (ESA) remote sensing satellite ERS-1. The mesoscale feature images are from Norwegian coastal waters and the Mediterranean (Elba and Sicily areas). Theories are tested for their ability to explain the observed variability of the radar-cross section. By means of empirical models, developed for the ERS-1 scatterometer, wind speeds are extracted from the SAR images and compared with measured data. Theories of SAR imaging and boundary-layer stability are applied to investigating the imaging of thermal fronts. The possibility of determining surface-current variability from SAR images is emphasized. The theoretical approach is based on the modulation of small-scale scattering waves by underlying currents.

Keywords

C-band SAR – coastal oceanography – ERS-1 – surface current
surface wind – thermal fronts

Issuing Organization

Initial Distribution for SR-247

Ministries of Defence		_SCNR for SACLANTCEN_	
DND Canada	10	SCNR Belgium	1
CHOD Denmark	8	SCNR Canada	1
MOD Germany	15	SCNR Denmark	1
HNDGS Greece	12	SCNR Germany	1
MARISTAT Italy	10	SCNR Greece	1
MOD (Navy) Netherlands	12	SCNR Italy	1
NDRE Norway	10	SCNR Netherlands	1
MOD Spain	2	SCNR Norway	1
MDN Portugal	5	SCNR Portugal	1
TDKK Turkey	5	SCNR Spain	1
MOD UK	20	SCNR Turkey	1
ONR US	49	SCNR UK	1
		SCNR US	2
		SECGEN Rep. SCNR	1
		NAMILCOM Rep. SCNR	1

NATO Authorities			
NAMILCOM	2		
SACLANT	3		
CINCEASTLANT/ COMNAVNORTHWEST	1	_National Liaison Officers_	
CINCIBERLANT	1	NLO Canada	1
CINCWESTLANT	1	NLO Denmark	1
COMASWSTRIKFOR	1	NLO Germany	1
COMMAIREASTLANT	1	NLO Italy	1
COMSTRIKFLTANT	1	NLO Netherlands	1
COMSUBACLANT	1	NLO UK	1
SACLANTREPEUR	1	NLO US	1
SACEUR	2		
CINCNORTHWEST	1		
CINCSOUTH	1		
COMEDCENT	1		
COMMARAIRMED	1		
COMNAVSOUTH	1		
COMSTRIKFORSOUTH	1		
COMSUBMED	1	Total external distribution	205
SHAPE Technical Centre	1	SACLANTCEN Library	20
PAT	1		
		Total number of copies	225